Chapter 3
Simulation-Driven Design in Microwave Engineering: Application Case Studies

Slawomir Koziel and Stanislav Ogurtsov

Abstract. Application of surrogate-based optimization methods to simulation-driven microwave engineering design is demonstrated. It is essential for the considered techniques that the optimization of the original high-fidelity EM-simulated model is replaced by the iterative optimization of its computationally cheap surrogate. The surrogate is updated using available high-fidelity model data to maintain its prediction capability throughout the optimization process. The surrogate model is constructed from the low-fidelity model which—depending on a particular application case—can be either an equivalent circuit or a coarsely discretized full-wave electromagnetic model. Designs satisfying performance requirements are typically obtained at the cost of just a few evaluations of the high-fidelity model. Here, several surrogate-based design optimization techniques for the use in microwave engineering are discussed. Applications of space mapping, simulation-based tuning, variable-fidelity optimization, as well as various response correction techniques are illustrated. Design examples include planar filters, antennas, and transmission line transitions structures.

Keywords: computer-aided design (CAD), microwave design, simulation-driven optimization, electromagnetic (EM) simulation, surrogate-based optimization, space mapping, tuning, surrogate model, high-fidelity model, coarse model.

3.1 Introduction

In this chapter, first, we describe several simulation-driven design optimization methods exploiting physically-based surrogate models, which can be used to

Slawomir Koziel · Stanislav Ogurtsov
Engineering Optimization & Modeling Center, School of Science and Engineering, Reykjavik University, Menntavegur 1, Reykjavik, 101, Iceland
e-mail: koziel@ru.is; stanislav@ru.is

X.-S. Yang & S. Koziel (Eds.): Computational Optimization & Applications, SCI 359, pp. 57–97.
springerlink.com

design a variety of microwave structures and devices in a computationally efficient way. Second, we illustrate application of these surrogate-based optimization methods for design of microwave components. Examples include a variety of structures such as microstrip filters, ultrawide band (UWB) antenna, planar Yagi antenna, broadband antenna on multilayer substrate, low-loss transition from coplanar waveguide to microstrip and substrate integrated waveguide. All these design problems are computationally expensive so that application of conventional simulation-driven techniques (e.g., gradient-based algorithms) is not practical or even unfeasible. It will be demonstrated that the surrogate based methods exploiting the physically-based low-fidelity models can generate satisfactory designs at the cost corresponding to a few high-fidelity electromagnetic (EM) simulations of the structure of interest.

3.2 Surrogate-Based Design Optimization in Microwave Engineering

Microwave design task can be formulated as a nonlinear minimization problem

$$\boldsymbol{x}^* \in \arg\min_{\boldsymbol{x} \in X_f} U\left(\boldsymbol{R}_f(\boldsymbol{x})\right) \tag{3.1}$$

where $\boldsymbol{R}_f \in R^m$ denotes the response vector of the device of interest, e.g., the modulus of the transmission coefficient $|S_{21}|$ evaluated at m different frequencies. U is a given scalar merit function, e.g., a minimax function with upper and lower specifications [1]. Vector $\boldsymbol{x}^*$ is the optimal design to be determined. Normally, $\boldsymbol{R}_f$ is obtained through computationally expensive electromagnetic simulation. It is referred to as the high-fidelity or fine model.

The conventional way of handling the design problem (3.1) is to employ the EM simulator directly within the optimization loop. This direct approach faces some fundamental difficulties. The most important one is the high computational cost of high-fidelity EM simulation which makes the optimization impractical. Another difficulty is that the responses obtained through EM simulation typically have poor analytical properties. In particular, EM-based objective functions are inherently noisy. Additional problem for direct EM-based optimization is that the sensitivity information may not be available or expensive to compute. Only recently, computationally cheap adjoint sensitivities [2] started to become available in some major commercial EM simulation packages, although for frequency-domain solvers only [3], [4].

Computationally efficient simulation-driven design can be performed using surrogate models. Microwave design through surrogate-based optimization (SBO) [1], [5], [6] is the main focus of this chapter. The primary reason for using SBO approach in microwave engineering is to speed up the design process by shifting the optimization burden to an inexpensive yet reasonably accurate surrogate model of the device.

The generic SBO framework described here that the direct optimization of the computationally expensive EM-simulated high-fidelity model $\boldsymbol{R}_f$ is replaced by an iterative procedure [1], [6]

$$\boldsymbol{x}^{(i+1)} = \arg\min_{\boldsymbol{x}} U\left(\boldsymbol{R}_s^{(i)}(\boldsymbol{x})\right) \tag{3.2}$$

that generates a sequence of points (designs) $\boldsymbol{x}^{(i)} \in X_f$, $i = 0, 1, \ldots$, being approximate solutions to the original design problem (3.1). Each $\boldsymbol{x}^{(i+1)}$ is the optimal design of the surrogate model $\boldsymbol{R}_s^{(i)}: X_s^{(i)} \rightarrow R^m$, $X_s^{(i)} \subseteq R^n$, $i = 0, 1, \ldots$. $\boldsymbol{R}_s^{(i)}$ is assumed to be a computationally cheap and sufficiently reliable representation of the fine model $\boldsymbol{R}_f$, particularly in the neighborhood of the current design $\boldsymbol{x}^{(i)}$. Under these assumptions, the algorithm (3.2) is likely to produce a sequence of designs that quickly approach $\boldsymbol{x}_f^*$.

Typically, $\boldsymbol{R}_f$ is only evaluated once per iteration (at every new design $\boldsymbol{x}^{(i+1)}$) for verification purposes and to obtain the data necessary to update the surrogate model. Since the surrogate model is computationally cheap, its optimization cost (cf. (2)) can usually be neglected and the total optimization cost is determined by the evaluation of $\boldsymbol{R}_f$. The key point here is that the number of evaluations of $\boldsymbol{R}_f$ for a well performing surrogate-based algorithm is substantially smaller than for any direct optimization method (e.g., gradient-based one) [7].

In the remaining part of this section we characterize the surrogate models used in microwave engineering (Section 3.2.1) and present several techniques for computationally efficient simulation-driven design of microwave structures (Sections 3.2.2 through 3.2.6). Discussion covers the following methods: space mapping [1], [7], simulation-based tuning [8], shape-preserving response prediction [9], variable-fidelity optimization [10], as well as optimization through adaptively adjusted design specifications [11].

3.2.1 Surrogate Models in Microwave Engineering

There are a number of ways to create surrogate models of microwave and radio-frequency (RF) devices and structures. They can be classified into two groups: functional and physical surrogates. Functional models are constructed from sampled high-fidelity model data using suitable function approximation techniques (e.g., polynomial regression [5] or kriging [5]). Physical surrogates exploit fast but limited-accuracy models that are physically related to the original structure under consideration.

Here, we focus on methods exploiting physical surrogates. Their primary advantage is that they are typically able to ensure good accuracy and generalization capability while using only a few training data points [12]. Physical surrogates are based on underlying physically-based low-fidelity models of the structure of interest (denoted here as $\boldsymbol{R}_c$). Physically-based models describe the same physical phenomena as the high-fidelity model, however, in a simplified manner. In microwave engineering, the high-fidelity model describes behavior of the system in terms of the distributions of the electric and magnetic fields within (and,

sometimes in its surrounding) that are calculated by solving the corresponding set of Maxwell equations [13]. Furthermore, the system performance is expressed through certain characteristics related to its input/output ports (such as so-called *S*-parameters [13]). All of these are obtained as a result of high-resolution electromagnetic simulation where the structure under consideration is finely discretized. In this context, the physically-based low-fidelity model of the microwave device can be obtained through: (i) analytical description of the structure using theory-based or semi-empirical formulas, (ii) different level of physical description of the system. The typical example in microwave engineering is equivalent circuit [1], where the device of interest is represented using lumped components (inductors, capacitors, microstrip line models, etc.), (iii) low-fidelity electromagnetic simulation. This approach allows us to use the same EM solver to evaluate both the high- and low-fidelity models; however, the latter is using much coarser simulation mesh which results in degraded accuracy but much shorter simulation time. The properties of the three groups of models are summarized in Table 3.1.

Table 3.1 Physically-based low-fidelity models in microwave engineering

Model Type	CPU Cost	Accuracy	Availability
Analytical	Very cheap	Low	Rather limited
Equivalent circuit	Cheap	Decent	Limited (mostly filters)
Coarsely-discretized EM simulation	Expensive	Good to very good	Generic: available for all structures

3.2.2 Space Mapping

Space mapping (SM) [1], [7] is probably one of the most recognized SBO techniques using physically-based low-fidelity (or coarse) models in microwave engineering. SM exploits the algorithm (3.2) to generate a sequence of approximate solutions $\boldsymbol{x}^{(i)}$, $i = 0, 1, 2, \ldots$, to problem (3.1). The surrogate model at iteration i, $\boldsymbol{R}_s^{(i)}$, is constructed from the low-fidelity model so that the misalignment between $\boldsymbol{R}_s^{(i)}$ and the fine model is minimized using so-called parameter extraction process, which is the nonlinear minimization problem by itself [1]. The surrogate is defined as [7]

$$\boldsymbol{R}_s^{(i)}(\boldsymbol{x}) = \boldsymbol{R}_{s.g}(\boldsymbol{x}, \boldsymbol{p}^{(i)}) \tag{3.3}$$

where $\boldsymbol{R}_{s.g}$ is a generic space mapping surrogate model, i.e., the low-fidelity model composed with suitable transformations, whereas

$$\boldsymbol{p}^{(i)} = \arg\min_{\boldsymbol{p}} \sum_{k=0}^{i} w_{i.k} \, \| \boldsymbol{R}_f(\boldsymbol{x}^{(k)}) - \boldsymbol{R}_{s.g}(\boldsymbol{x}^{(k)}, \boldsymbol{p}) \| \tag{3.4}$$

is a vector of model parameters and $w_{i.k}$ are weighting factors; a common choice of $w_{i.k}$ is $w_{i.k} = 1$ for all i and all k.

Various space mapping surrogate models are available [1], [7]. They can be roughly categorized into four groups: (i) Models based on a (usually linear) distortion of coarse model parameter space, e.g., input space mapping of the form $\boldsymbol{R}_{s.g}(\boldsymbol{x}, \boldsymbol{p}) = \boldsymbol{R}_{s.g}(\boldsymbol{x}, \boldsymbol{B}, \boldsymbol{c}) = \boldsymbol{R}_c(\boldsymbol{B}\cdot\boldsymbol{x} + \boldsymbol{c})$ [1]; (ii) Models based on a distortion of the coarse model response, e.g., output space mapping of the form $\boldsymbol{R}_{s.g}(\boldsymbol{x}, \boldsymbol{p}) = \boldsymbol{R}_{s.g}(\boldsymbol{x}, \boldsymbol{d}) = \boldsymbol{R}_c(\boldsymbol{x}) + \boldsymbol{d}$ [7]; (iii) Implicit space mapping, where the parameters used to align the surrogate with the fine model are separate from the design variables, i.e., $\boldsymbol{R}_{s.g}(\boldsymbol{x}, \boldsymbol{p}) = \boldsymbol{R}_{s.g}(\boldsymbol{x}, \boldsymbol{x}_p) = \boldsymbol{R}_{c.i}(\boldsymbol{x}, \boldsymbol{x}_p)$, with $\boldsymbol{R}_{c.i}$ being the coarse model dependent on both the design variables $\boldsymbol{x}$ and so-called preassigned parameters $\boldsymbol{x}_p$ (e.g., dielectric constant, substrate height) that are normally fixed in the fine model but can be freely altered in the coarse model [30]; (iv) Custom models exploiting parameters characteristic to a given design problem; the most characteristic example is the so-called frequency space mapping $\boldsymbol{R}_{s.g}(\boldsymbol{x}, \boldsymbol{p}) = \boldsymbol{R}_{s.g}(\boldsymbol{x}, \boldsymbol{F}) = \boldsymbol{R}_{c.f}(\boldsymbol{x}, \boldsymbol{F})$ [1], where $\boldsymbol{R}_{c.f}$ is a frequency-mapped coarse model, i.e., the coarse model evaluated at frequencies different from the original frequency sweep for the fine model, according to the mapping $\omega \rightarrow f_1 + f_2\omega$, with $\boldsymbol{F} = [f_1 \ f_2]^T$.

A though discussion of various issues as well as generalizations of space mapping can be found in the literature [12, 14, 15].

3.2.3 Simulation-Based Tuning and Tuning Space Mapping

Tuning space mapping (TSM) [8] combines the concept of tuning, widely used in microwave engineering [16], [17], and space mapping. It is an iterative optimization procedure that assumes the existence of two surrogate models: both are less accurate but computationally much cheaper than the fine model. The first model is a so-called tuning model $\boldsymbol{R}_t$ that contains relevant fine model data (typically a fine model response) at the current iteration point and tuning parameters (typically implemented through circuit elements inserted into tuning ports). The tunable parameters are adjusted so that the model $\boldsymbol{R}_t$ satisfies the design specifications. The second model, $\boldsymbol{R}_c$ is used for calibration purposes: it allows us to translate the change of the tuning parameters into relevant changes of the actual design variables; $\boldsymbol{R}_c$ is dependent on three sets of variables: design parameters, tuning parameters (which are actually the same parameters as the ones used in $\boldsymbol{R}_t$), and SM parameters that are adjusted using the usual parameter extraction process [1] in order to have the model $\boldsymbol{R}_c$ meet certain matching conditions. Typically, the model $\boldsymbol{R}_c$ is a standard SM surrogate (i.e., a coarse model composed with suitable transformations) enhanced by the same or corresponding tuning elements as the model $\boldsymbol{R}_t$. The conceptual illustrations of the fine model, the tuning model and the calibration model are shown in Fig. 3.1.

The iteration of the TSM algorithm consists of two steps: optimization of the tuning model and a calibration procedure. First, the current tuning model $\boldsymbol{R}_t^{(i)}$ is built using fine model data at point $\boldsymbol{x}^{(i)}$. In general, because the fine model with inserted tuning ports is not identical to the original structure, the tuning model response may not agree with the response of the fine model at $\boldsymbol{x}^{(i)}$ even if the values

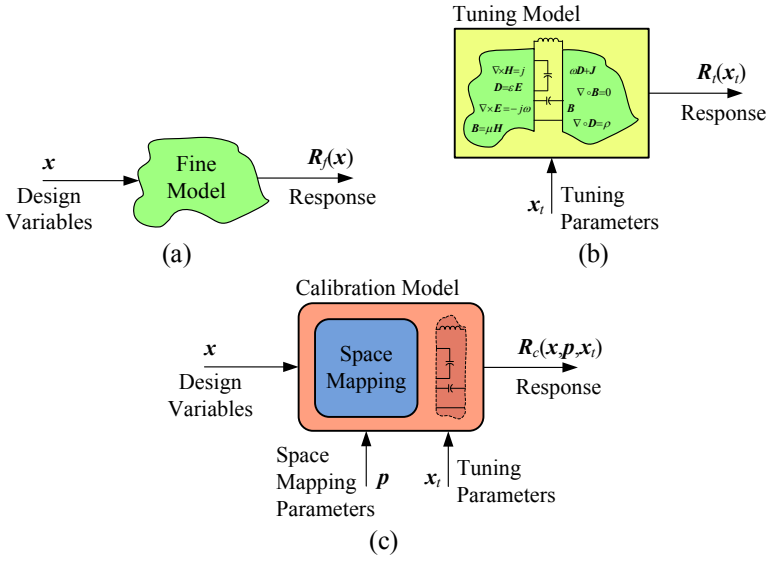

Fig. 3.1 Conceptual illustrations of the fine model, the tuning model and the calibration model: (a) the fine model is typically based on full-wave simulation, (b) the tuning model exploits the fine model "image" (e.g., in the form of *S*-parameters corresponding to the current design imported to the tuning model using suitable data components) and a number of circuit-theory-based tuning elements, (c) the calibration model is usually a circuit equivalent dependent on the same design variables as the fine model, the same tuning parameters as the tuning model and, additionally, a set of space mapping parameters used to align the calibration model with both the fine and the tuning model during the calibration process.

of the tuning parameters $\boldsymbol{x}_t$ are zero, so that these values must be adjusted to, say, $\boldsymbol{x}_{t.0}{}^{(i)}$, in order to obtain alignment [8]:

$$\boldsymbol{x}_{t.0}^{(i)} = \arg\min_{\boldsymbol{x}_t} \left\| \boldsymbol{R}_f(\boldsymbol{x}^{(i)}) - \boldsymbol{R}_t^{(i)}(\boldsymbol{x}_t) \right\| \tag{3.5}$$

In the next step, one optimizes $\boldsymbol{R}_t^{(i)}$ to have it meet the design specifications. Optimal values of the tuning parameters $\boldsymbol{x}_{t.1}{}^{(i)}$ are obtained as follows:

$$\boldsymbol{x}_{t.1}^{(i)} = \arg\min_{\boldsymbol{x}_t} U\left(\boldsymbol{R}_t^{(i)}(\boldsymbol{x}_t)\right) \tag{3.6}$$

Having $\boldsymbol{x}_{t.1}{}^{(i)}$, the calibration procedure is performed to determine changes in the design variables that yield the same change in the calibration model response as that caused by $\boldsymbol{x}_{t.1}{}^{(i)} - \boldsymbol{x}_{t.0}{}^{(i)}$ [8]. First one adjusts the SM parameters $\boldsymbol{p}^{(i)}$ of the calibration model to obtain a match with the fine model response at $\boldsymbol{x}^{(i)}$

$$\boldsymbol{p}^{(i)} = \arg\min_{\boldsymbol{p}} \left\| \boldsymbol{R}_f(\boldsymbol{x}^{(i)}) - \boldsymbol{R}_c(\boldsymbol{x}^{(i)}, \boldsymbol{p}, \boldsymbol{x}_{t.0}^{(i)}) \right\|. \tag{3.7}$$

The calibration model is then optimized with respect to the design variables in order to obtain the next iteration point $\boldsymbol{x}^{(i+1)}$

$$\boldsymbol{x}^{(i+1)} = \arg\min_{\boldsymbol{x}} \left\| \boldsymbol{R}_t^{(i)}(\boldsymbol{x}_{t.1}^{(i)}) - \boldsymbol{R}_c(\boldsymbol{x}, \boldsymbol{p}^{(i)}, \boldsymbol{x}_{t.0}^{(i)}) \right\|. \tag{3.8}$$

Note that $\boldsymbol{x}_{t.0}{}^{(i)}$ is used in (3.7), which corresponds to the state of the tuning model after performing the alignment procedure (3.5), and $\boldsymbol{x}_{t.1}{}^{(i)}$ in (3.8), which corresponds to the optimized tuning model (cf. (6)). Thus, (3.7) and (3.8) allow finding the change of design variable values $\boldsymbol{x}^{(i+1)} - \boldsymbol{x}^{(i)}$ necessary to compensate the effect of changing the tuning parameters from $\boldsymbol{x}_{t.0}{}^{(i)}$ to $\boldsymbol{x}_{t.1}{}^{(i)}$.

Thorough discussion of various variations of tuning space mapping algorithms, calibration procedures, as well as recent development in the TSM technology can be found in the literature [18, 19, 20].

3.2.4 Shape-Preserving Response Prediction

Shape-preserving response prediction (SPRP) [9] is a response correction technique that takes advantage of the similarity between responses of the high- and low-fidelity models in a very straightforward way. SPRP assumes that the change of the high-fidelity model response due to the adjustment of the design variables can be predicted using the actual changes of the low-fidelity model response. Therefore, it is critically important that the low-fidelity model is physically based, which ensures that the effect of the design parameter variations on the model response is similar for both models. In microwave engineering this property is likely to hold, particularly if the low-fidelity model is the coarsely-discretization structure evaluated using the same EM solver as the one used to simulate the high-fidelity model.

The change of the low-fidelity model response is described by the translation vectors corresponding to a certain (finite) number of characteristic points of the model's response. These translation vectors are subsequently used to predict the change of the high-fidelity model response with the actual response of $\boldsymbol{R}_f$ at the current iteration point, $\boldsymbol{R}_f(\boldsymbol{x}^{(i)})$, treated as a reference.

Figure 3.2(a) shows the example low-fidelity model response, $|S_{21}|$ in the frequency range 8 GHz to 18 GHz, at the design $\boldsymbol{x}^{(i)}$, as well as the low-fidelity model response at some other design $\boldsymbol{x}$. The responses come from the double folded stub bandstop filter example considered in [9]. Circles denote characteristic points of $\boldsymbol{R}_c(\boldsymbol{x}^{(i)})$, selected here to represent $|S_{21}| = -3$ dB, $|S_{21}| = -20$ dB, and the local $|S_{21}|$ maximum (at about 13 GHz). Squares denote corresponding characteristic points for $\boldsymbol{R}_c(\boldsymbol{x})$, while line segments represent the translation vectors ("shift") of the characteristic points of $\boldsymbol{R}_c$ when changing the design variables from $\boldsymbol{x}^{(i)}$ to $\boldsymbol{x}$. Since the low-fidelity model is physically based, the high-fidelity model response at the given design, here, $\boldsymbol{x}$, can be predicted using the same translation vectors applied to the corresponding characteristic points of the high-fidelity model response at $\boldsymbol{x}^{(i)}$, $\boldsymbol{R}_f(\boldsymbol{x}^{(i)})$. This is illustrated in Fig. 3.2(b). Rigorous formulation of SPRP as well as generalizations of the basic algorithm can be found in [9].

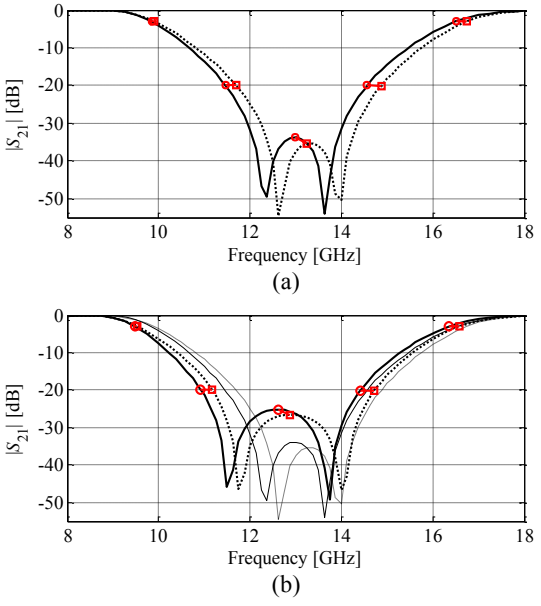

Fig. 3.2 SPRP concept: (a) Example low-fidelity model response at the design $\boldsymbol{x}^{(i)}$, $\boldsymbol{R}_c(\boldsymbol{x}^{(i)})$ (solid line), the low-fidelity model response at $\boldsymbol{x}$, $\boldsymbol{R}_c(\boldsymbol{x})$ (dotted line), characteristic points of $\boldsymbol{R}_c(\boldsymbol{x}^{(i)})$ (circles) and $\boldsymbol{R}_c(\boldsymbol{x})$ (squares), and the translation vectors (short lines); (b) High-fidelity model response at $\boldsymbol{x}^{(i)}$, $\boldsymbol{R}_f(\boldsymbol{x}^{(i)})$ (solid line) and the predicted high-fidelity model response at $\boldsymbol{x}$ (dotted line) obtained using SPRP based on characteristic points of Fig. 3.2(a); characteristic points of $\boldsymbol{R}_f(\boldsymbol{x}^{(i)})$ (circles) and the translation vectors (short lines) were used to find the characteristic points (squares) of the predicted high-fidelity model response; low-fidelity model responses $\boldsymbol{R}_c(\boldsymbol{x}^{(i)})$ and $\boldsymbol{R}_c(\boldsymbol{x})$ are plotted using thin solid and dotted line, respectively [9].

3.2.5 Multi-fidelity Optimization Using Coarse-Discretization EM Models

The most versatile type of physically-based low-fidelity model in microwave engineering is the one obtained through EM simulation of coarsely-discretized structure of interest. The computational cost of the model and its accuracy can be easily controlled by changing the discretization density. This feature has been exploited in the multi-fidelity optimization algorithm introduced in [10].

The design optimization methodology of [10] is based on a family of coarse-discretization models $\{\boldsymbol{R}_{c.j}\}$, $j = 1,\ldots, K$, all evaluated by the same EM solver as the one used for the high-fidelity model. Discretization of the model $\boldsymbol{R}_{c.j+1}$ is finer than that of the model $\boldsymbol{R}_{c.j}$, which results in better accuracy but also longer evaluation time. In practice, the number of coarse-discretization models is two or three.

Having the optimized design $\boldsymbol{x}^{(K)}$ of the last (and finest) coarse-discretization model $\boldsymbol{R}_{c.K}$, the model is evaluated at all perturbed designs around $\boldsymbol{x}^{(K)}$, i.e., at $\boldsymbol{x}_k^{(K)} = [x_1^{(K)} \ \ldots \ x_k^{(K)} + \text{sign}(k)\cdot d_k \ \ldots \ x_n^{(K)}]^T$, $k = -n, -n+1, \ldots, n-1, n$. A notation of $\boldsymbol{R}^{(k)} =$

$\boldsymbol{R}_{c.K}(\boldsymbol{x}_k^{(K)})$ is adopted here. This data can be used to refine the final design without directly optimizing $\boldsymbol{R}_f$. Instead, an approximation model involving $\boldsymbol{R}^{(k)}$ is set up and optimized in the neighborhood of $\boldsymbol{x}^{(K)}$ defined as $[\boldsymbol{x}^{(K)} - \boldsymbol{d}, \boldsymbol{x}^{(K)} + \boldsymbol{d}]$, where $\boldsymbol{d} = [d_1\ d_2\ \ldots\ d_n]^T$. The size of the neighborhood can be selected based on sensitivity analysis of $\boldsymbol{R}_{c.1}$ (the cheapest of the coarse-discretization models); usually $\boldsymbol{d}$ equals 2 to 5 percent of $\boldsymbol{x}^{(K)}$.

Here, the approximation is performed using a reduced quadratic model $\boldsymbol{q}(\boldsymbol{x}) = [q_1\ q_2\ \ldots\ q_m]^T$, defined as

$$q_j(\boldsymbol{x}) = q_j([x_1 \ldots x_n]^T) = \lambda_{j.0} + \lambda_{j.1}x_1 + \ldots + \lambda_{j.n}x_n + \lambda_{j.n+1}x_1^2 + \ldots + \lambda_{j.2n}x_n^2 \tag{3.9}$$

Coefficients $\lambda_{j.r}$, $j = 1, \ldots, m$, $r = 0, 1, \ldots, 2n$, can be uniquely obtained by solving the linear regression problems

$$\begin{bmatrix} 1 & x_{-n.1}^{(K)} & \cdots & x_{-n.n}^{(K)} & (x_{-n.1}^{(K)})^2 & \cdots & (x_{-n.n}^{(K)})^2 \\ \vdots & \vdots & & \vdots & & \vdots & \vdots \\ 1 & x_{0.1}^{(K)} & \cdots & x_{0.n}^{(K)} & (x_{0.1}^{(K)})^2 & \cdots & (x_{-n.n}^{(K)})^2 \\ \vdots & \vdots & & \vdots & & \vdots & \vdots \\ 1 & x_{n.1}^{(K)} & \cdots & x_{n.n}^{(K)} & (x_{n.1}^{(K)})^2 & \cdots & (x_{-n.n}^{(K)})^2 \end{bmatrix} \cdot \begin{bmatrix} \lambda_{j.0} \\ \lambda_{j.1} \\ \vdots \\ \lambda_{j.2n} \end{bmatrix} = \begin{bmatrix} R_j^{(-n)} \\ \vdots \\ R_j^{(0)} \\ \vdots \\ R_j^{(n)} \end{bmatrix} \tag{3.10}$$

where $x_{k.j}^{(K)}$ is a jth component of the vector $\boldsymbol{x}_k^{(K)}$, and $R_j^{(k)}$ is a jth component of the vector $\boldsymbol{R}^{(k)}$, i.e.,

In order to account for unavoidable misalignment between $\boldsymbol{R}_{c.K}$ and $\boldsymbol{R}_f$, instead of optimizing the quadratic model $\boldsymbol{q}$, it is recommended to optimize a corrected model $\boldsymbol{q}(\boldsymbol{x}) + [\boldsymbol{R}_f(\boldsymbol{x}^{(K)}) - \boldsymbol{R}_{c.K}(\boldsymbol{x}^{(K)})]$ that ensures a zero-order consistency [21] between $\boldsymbol{R}_{c.K}$ and $\boldsymbol{R}_f$. The refined design can be then found as

$$\boldsymbol{x}^* = \arg\min_{\boldsymbol{x}^{(K)} - \boldsymbol{d} \le \boldsymbol{x} \le \boldsymbol{x}^{(K)} + \boldsymbol{d}} U(\boldsymbol{q}(\boldsymbol{x}) + [\boldsymbol{R}_f(\boldsymbol{x}^{(K)}) - \boldsymbol{R}_{c.K}(\boldsymbol{x}^{(K)})]) \tag{3.11}$$

This kind of correction is also known as output space mapping [7]. If necessary, the step (4) can be performed a few times starting from a refined design, i.e., $\boldsymbol{x}^* = \text{argmin}\{\boldsymbol{x}^{(K)} - \boldsymbol{d} \le \boldsymbol{x} \le \boldsymbol{x}^{(K)} + \boldsymbol{d} : U(\boldsymbol{q}(\boldsymbol{x}) + [\boldsymbol{R}_f(\boldsymbol{x}^*) - \boldsymbol{R}_{c.K}(\boldsymbol{x}^*)])\}$ (each iteration requires only one evaluation of $\boldsymbol{R}_f$).

The design optimization procedure can be summarized as follows (input arguments are: initial design $\boldsymbol{x}^{(0)}$ and the number of coarse-discretization models K):

1. Set $j = 1$;
2. Optimize coarse-discretization model $\boldsymbol{R}_{c.j}$ to obtain a new design $\boldsymbol{x}^{(j)}$ using $\boldsymbol{x}^{(j-1)}$ as a starting point;
3. Set $j = j + 1$; if $j < K$ go to 2;
4. Obtain a refined design $\boldsymbol{x}^*$ as in (3.13);
5. END;

Note that the original model $\boldsymbol{R}_f$ is only evaluated at the final stage (step 4) of the optimization process. Operation of the algorithm in illustrated in Fig. 3.3. Coarse-discretization models can be optimized using any available algorithm.

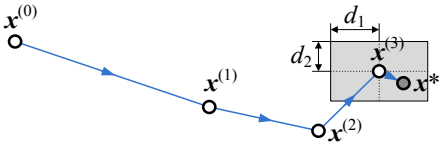

Fig. 3.3 Operation of the multi-fidelity design optimization procedure for $K = 3$ (three coarse-discretization models). The design $\boldsymbol{x}^{(j)}$ is obtained as the optimal solution of the model $\boldsymbol{R}_{c.j}$, $j = 1, 2, 3$. A reduced second-order approximation model $\boldsymbol{q}$ is set up in the neighborhood of $\boldsymbol{x}^{(3)}$ (gray area) and the final design $\boldsymbol{x}^*$ is obtained by optimizing a reduced $\boldsymbol{q}$ as in (3.13).

3.2.6 Optimization Using Adaptively Adjusted Design Specifications

The techniques described in Section 3.2.2 to 3.2.5 aimed at correcting the low-fidelity model so that it becomes, at least locally, an accurate representation of the high-fidelity model. An alternative way of exploiting low-fidelity models in simulation-driven design of microwave structures is to modify the design specifications in such a way that the updated specifications reflect the discrepancy between the models. This approach is extremely simple to implement because no changes of the low-fidelity model are necessary.

The adaptively adjusted design specifications optimization procedure introduced in [11] consists of the following two simple steps that can be iterated if necessary:

1. Modify the original design specifications in order to take into account the difference between the responses of $\boldsymbol{R}_f$ and $\boldsymbol{R}_c$ at their characteristic points.
2. Obtain a new design by optimizing the coarse model with respect to the modified specifications.

Characteristic points of the responses should correspond to the design specification levels. They should also include local maxima/minima of the respective responses at which the specifications may not be satisfied. Figure 3.4(a) shows fine and coarse model response at the optimal design of $\boldsymbol{R}_c$, corresponding to the bandstop filter example considered in [11]; design specifications are indicated using horizontal lines. Figure 3.4(b) shows characteristic points of $\boldsymbol{R}_f$ and $\boldsymbol{R}_c$ for the bandstop filter example. The points correspond to –3 dB and –30 dB levels as well to the local maxima of the responses. As one can observe in Fig. 3.4(b) the selection of points is rather straightforward.

In the first step of the optimization procedure, the design specifications are modified (or mapped) so that the level of satisfying/violating the modified specifications by the coarse model response corresponds to the satisfaction/violation levels of the original specifications by the fine model response. Modified design specifications are shown in Fig. 3.4(c).

The coarse model is subsequently optimized with respect to the modified specifications and the new design obtained this way is treated as an approximated solution to the original design problem (i.e., optimization of the fine model with

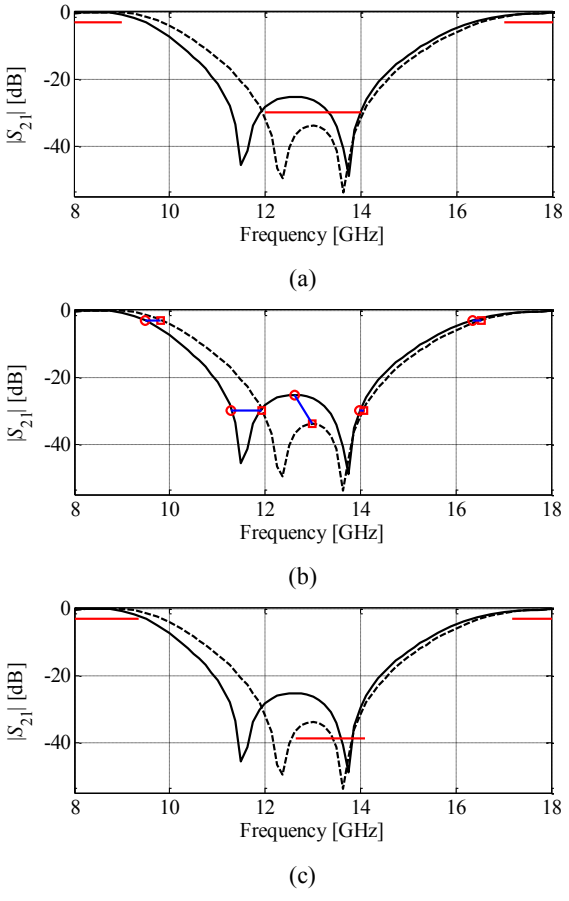

Fig. 3.4 Bandstop filter example (responses of $\boldsymbol{R}_f$ and $\boldsymbol{R}_c$ are marked with solid and dashed line, respectively) [11]: (a) fine and coarse model responses at the initial design (optimum of $\boldsymbol{R}_c$) as well as the original design specifications, (b) characteristic points of the responses corresponding to the specification levels (here, –3 dB and –30 dB) and to the local response maxima, (c) fine and coarse model responses at the initial design and the modified design specifications.

respect to the original specifications). Steps 1 and 2 (listed above) can be repeated if necessary. Substantial design improvement is typically observed after the first iteration, however, additional iterations may bring further enhancement [11].

In the first step of the optimization procedure, the design specifications are modified (or mapped) so that the level of satisfying/violating the modified specifications by the coarse model response corresponds to the satisfaction/violation levels of the original specifications by the fine model response. It is assumed that the coarse model is physically-based, in particular, that the adjustment of the design variables has similar effect on the response for both $\boldsymbol{R}_f$ and $\boldsymbol{R}_c$. In such a case the

coarse model design that is obtained in the second stage of the procedure (i.e., optimal with respect to the modified specifications) will be (almost) optimal for $\boldsymbol{R}_f$ with respect to the original specifications. As shown in Fig. 3.4, the absolute matching between the models is not as important as the shape similarity.

3.3 Surrogate-Based Design Optimization of Microwave Filters

In this section, three examples of microwave filter design using various surrogate-based optimization techniques are presented. A common feature of these three cases is that the surrogate model is created exploiting equivalent-circuit coarse model which is computationally much cheaper than the EM-simulated high-fidelity model. This results in a significant speedup of the optimization process.

3.3.1 Optimization of a Microstrip Bandpass Filter Using Space Mapping Technique

Consider the fourth-order ring resonator bandpass filter [22] shown in Fig. 3.5(a). The design parameters are $\boldsymbol{x} = [L_1\ L_2\ L_3\ S_1\ S_2\ W_1\ W_2]^T$ mm. The fine model $\boldsymbol{R}_f$ is simulated in the EM simulator FEKO [23]. The coarse model, Fig. 3.5(b), is an equivalent circuit implemented in Agilent ADS [24]. The design goal is to adjust the design variables so that the modulus of the transmission coefficient of the filter, $|S_{21}|$, satisfies the following requirements: $|S_{21}| \geq -1$ dB for 1.75 GHz $\leq f \leq$ 2.25 GHz, and $|S_{21}| \leq -20$ dB for 1.0 GHz $\leq f \leq$ 1.5GHz and 2.5 GHz $\leq f \leq$ 3.0 GHz, where f stands for frequency. The initial design is the coarse model optimal solution $\boldsymbol{x}^{(0)} = [24.74\ 19.51\ 24.10\ 0.293\ 0.173\ 1.232\ 0.802]^T$ mm (minimax specification error +9.0 dB).

Table 3.2 shows the optimization results. The surrogate model is constructed using input and output space mapping of the form $\boldsymbol{R}_s^{(i)}(\boldsymbol{x}) = \boldsymbol{R}_c^{(i)}(\boldsymbol{x} + \boldsymbol{c}^{(i)}) + \boldsymbol{d}^{(i)}$ [7], where $\boldsymbol{c}^{(i)}$ is obtained using the parameter extraction procedure [1], see also Section 3.2.2, eq. (3.4), whereas $\boldsymbol{d}^{(i)} = \boldsymbol{R}_f(\boldsymbol{x}^{(i)}) - \boldsymbol{R}_c(\boldsymbol{x}^{(i)} + \boldsymbol{c}^{(i)})$. Also an enhanced model of the form $\boldsymbol{R}_s^{(i)}(\boldsymbol{x}) = \boldsymbol{R}_c^{(i)}(\boldsymbol{x} + \boldsymbol{c}^{(i)}) + \boldsymbol{d}^{(i)} + \boldsymbol{E}^{(i)}(\boldsymbol{x} - \boldsymbol{x}^{(i)})$ is considered, where $\boldsymbol{E}^{(i)}$ is an approximation of the Jacobian of $\boldsymbol{R}_f(\boldsymbol{x}) - \boldsymbol{R}_c(\boldsymbol{x} + \boldsymbol{c}^{(i)})$ obtained using Broyden update [25]. The space mapping algorithm working with the enhanced surrogate uses trust-region convergence safeguard [25].

Figure 3.6 shows the initial fine model response and the optimized fine model response obtained using the algorithm with the enhanced surrogate model. Figure 3.7 shows the convergence plot for the both cases. For this example, the first version of the space mapping algorithm does not converge. Also, the final design is worse than the best one found in the course of optimization. This illustrates one of the difficulties of the standard SM technique: the algorithm does not ensure objective function improvement from iteration to iteration. The algorithm using approximated Jacobian and trust-regions exhibits better performance.

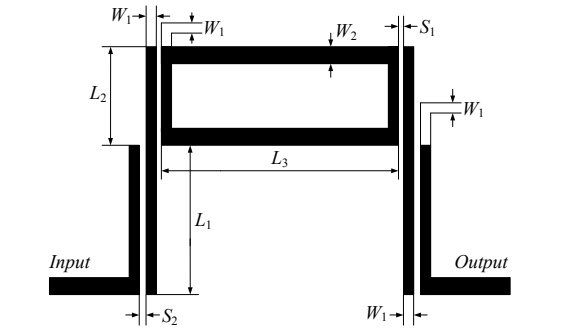

(a)

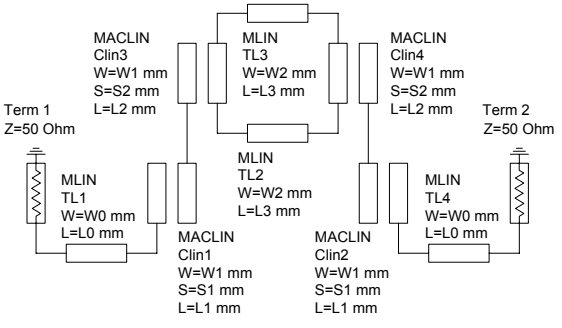

(b)

Fig. 3.5 Fourth-order ring resonator bandpass filter: (a) geometry [22], (b) coarse model (Agilent ADS).

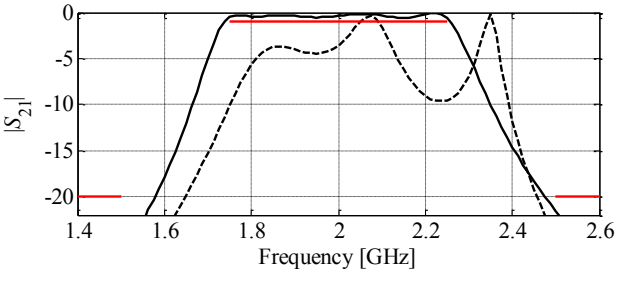

Fig. 3.6 Fourth-order ring resonator filter: Initial (dashed line) and optimized (solid line) $|S_{21}|$ versus frequency; optimization using $SM_{TR\text{-}B2}$ algorithm [25] with the $\boldsymbol{R}_c(\boldsymbol{x}+\boldsymbol{c})$ model: (a) full frequency range, (b) magnification at 1.4 GHz to 2.6 GHz and –22 dB to 0 dB.

Table 3.2 Fourth-order ring-resonator bandpass filter: optimization results

Surrogate Model	Spec. Error [dB]		Fine Model
	Final	Best Found	Runs [times]
$\boldsymbol{R}_s^{(i)}(\boldsymbol{x}) = \boldsymbol{R}_c^{(i)}(\boldsymbol{x} + \boldsymbol{c}^{(i)}) + \boldsymbol{d}^{(i)}$	–0.2	–0.3	21[#]
$\boldsymbol{R}_s^{(i)}(\boldsymbol{x}) = \boldsymbol{R}_c^{(i)}(\boldsymbol{x} + \boldsymbol{c}^{(i)}) + \boldsymbol{d}^{(i)} + \boldsymbol{E}^{(i)}(\boldsymbol{x} - \boldsymbol{x}^{(i)})$	–0.4	–0.4	17

[#] Convergence not obtained; algorithm terminated after 20 iterations.

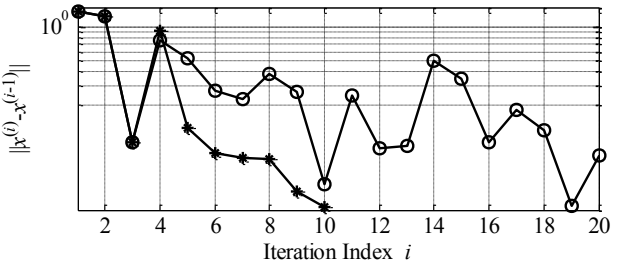

Fig. 3.7 Fourth-order ring resonator filter: convergence plots for the SM algorithm using surrogate model $\boldsymbol{R}_s^{(i)}(\boldsymbol{x}) = \boldsymbol{R}_c^{(i)}(\boldsymbol{x} + \boldsymbol{c}^{(i)}) + \boldsymbol{d}^{(i)}$ (o) and the algorithm using model $\boldsymbol{R}_s^{(i)}(\boldsymbol{x}) = \boldsymbol{R}_c^{(i)}(\boldsymbol{x} + \boldsymbol{c}^{(i)}) + \boldsymbol{d}^{(i)} + \boldsymbol{E}^{(i)}(\boldsymbol{x} - \boldsymbol{x}^{(i)})$.

3.3.2 Optimization of a Microstrip Bandpass Filter Using Tuning Space Mapping

Consider the box-section Chebyshev microstrip bandpass filter [26] (Fig. 3.8). The design parameters are $\boldsymbol{x} = [L_1\ L_2\ L_3\ L_4\ L_5\ S_1\ S_2]^T$. The fine model is simulated in Sonnet ***em*** [27] with a grid of 1 mil × 2 mil. The width parameters are $W = 40$ mil and $W_1 = 150$ mil. Substrate parameters are: relative permittivity $\varepsilon_r = 3.63$, and height $H = 20$ mil. The design specifications for the transmission coefficient are $|S_{21}| \le -20$ dB for 1.8 GHz $\le f \le$ 2.15 GHz and 2.65 GHz $\le f \le$ 3.0 GHz, and $|S_{21}| \ge -3$ dB for 2.4 GHz $\le f \le$ 2.5 GHz.

The filter is optimized using the tuning space mapping technology (Section 3.2.3). The tuning model is constructed by dividing the polygons corresponding to parameters L_1 to L_5 in the middle and inserting the tuning ports at the new cut edges. Its S28P data file (i.e., the file generated by the EM solver and containing the fine model *S*-parameter data) is then loaded into the *S*-parameter component in Agilent ADS [24]. The circuit-theory coupled-line components and capacitor components are chosen to be the tuning elements and are inserted into each pair of tuning ports (Fig. 3.9). The lengths of the imposed coupled-lines and the capacitances of the capacitors are assigned to be the tuning parameters, so that one has $\boldsymbol{x}_t = [L_{t1}\ L_{t2}\ L_{t3}\ L_{t4}\ L_{t5}\ C_{t1}\ C_{t2}]^T$ (L_{tk} in mil, C_{tk} in pF).

The calibration model is implemented in ADS and shown in Fig. 3.10. It contains the same tuning elements as the tuning model. It basically mimics the

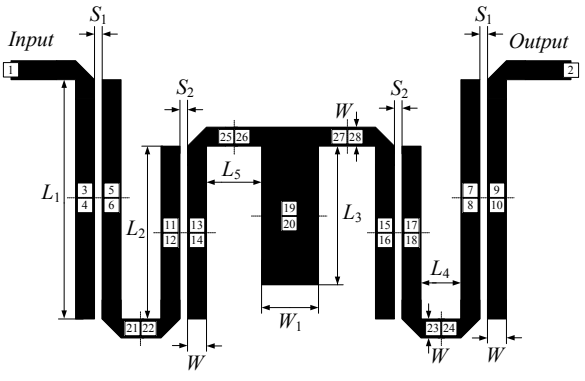

Fig. 3.8 Chebyshev bandpass filter: geometry [26], and the tuning port insertion points.

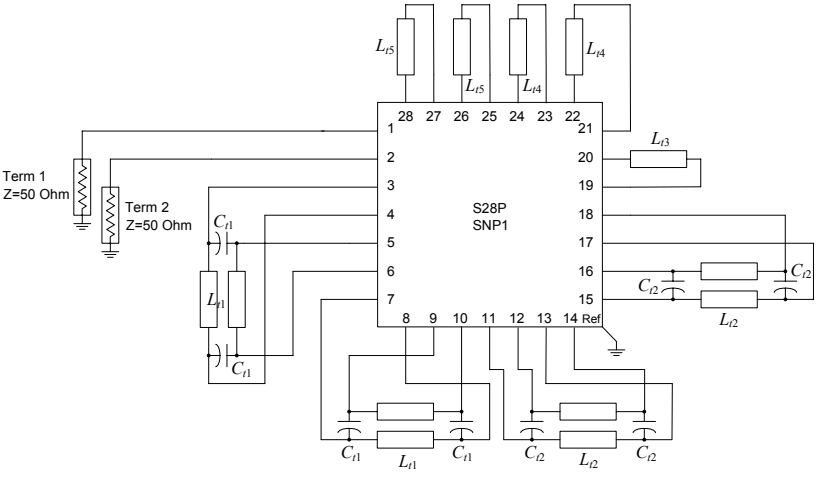

Fig. 3.9 Box-section Chebyshev bandpass filter: tuning model (Agilent ADS).

division of the coupled-lines performed while preparing $\boldsymbol{R}_t$. The calibration model also contains six (implicit) SM parameters that will be used as parameters $\boldsymbol{p}$ in the calibration process [8]. These parameters are $\boldsymbol{p} = [\varepsilon_{r1}\ \varepsilon_{r2}\ \varepsilon_{r3}\ \varepsilon_{r4}\ \varepsilon_{r5}\ H]^T$, where ε_{rk} is dielectric constant of the microstrip line segment of length L_k (Fig. 3.8), and H is the substrate height of the filter. Initial values of these parameters are $[3.63\ 3.63\ 3.63\ 3.63\ 3.63\ 20]^T$.

The initial design, $\boldsymbol{x}^{(0)} = [928\ 508\ 50\ 50\ 201\ 5\ 19]^T$ mil, is the optimal solution of the coarse model, i.e., the calibration model with zero values of the tuning parameters. The specification error is +19 dB.

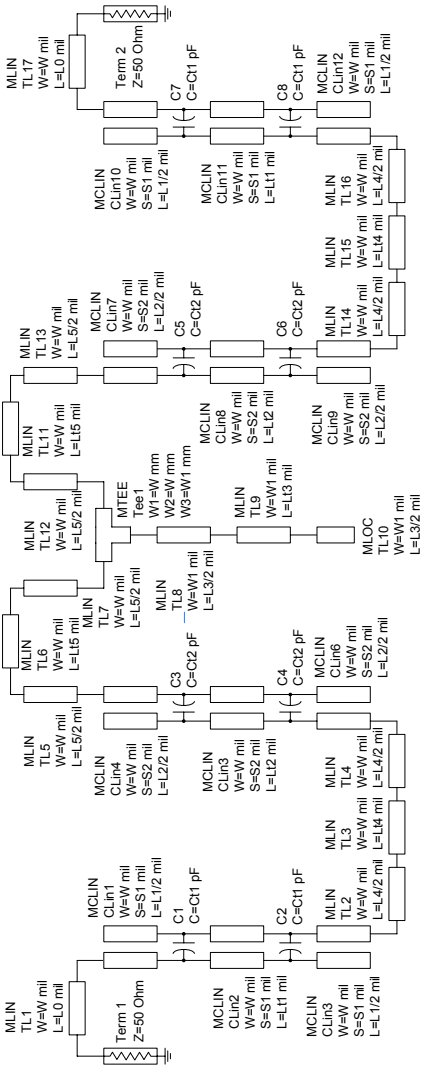

Fig. 3.10 Box-section Chebyshev bandpass filter: calibration model (Agilent ADS) [28].

The misalignment between the fine and the tuning model response with the tuning elements set to zero is negligible (thanks to the co-calibrated port feature in Sonnet ***em*** [8]) so that $\boldsymbol{x}_{t.0}^{(0)} = [0\ 0\ 0\ 0\ 0\ 0\ 0]^T$ was used throughout. The values of the tuning parameters at the optimal design of the tuning model are $\boldsymbol{x}_{t.1}^{(0)} = [-85.2\ 132.5\ 5.24\ 1.13\ -15.24\ 0.169\ -0.290]^T$. Note that some of the parameters take negative values, which is permitted in ADS. The values of preassigned parameters obtained in the first calibration phase [8] are $\boldsymbol{p}^{(0)} = [3.10\ 6.98\ 4.29\ 7.00\ 6.05\ 17.41]^T$.

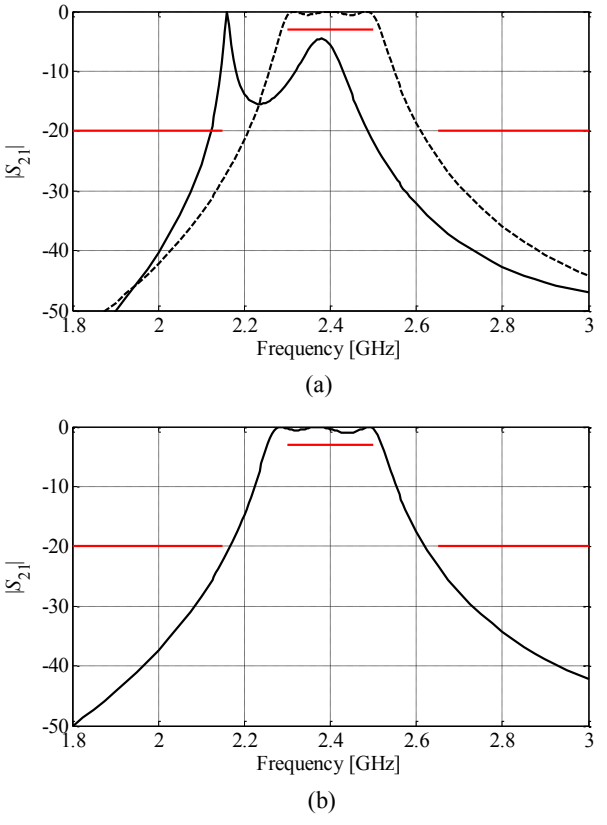

Fig. 3.11 Box-section Chebyshev bandpass filter: (a) the coarse (dashed line) and fine (solid line) model response at the initial design; (b) fine model response at the design found after one iteration of the TSM algorithm.

Figure 3.11 shows the coarse and fine model response at the initial design, as well as the fine model response after just one TSM iteration (two fine model evaluations) with $\boldsymbol{x}^{(1)} = [1022\ 398\ 46\ 56\ 235\ 4\ 10]^T$ mil (specification error –1.8 dB).

It should be emphasized that the evaluation time of both the tuning and the calibration model is very low (a fraction of a second), and, it is negligible compared to the evaluation time of the fine model. Therefore, the computational cost of each tuning space mapping iteration corresponds to two electromagnetic simulations (one for the fine model and one for the "cut" fine model).

3.3.3 Design of Dual-Band Bandpass Filter Using Shape-Preserving Response Prediction

To illustrate the performance of the shape-preserving response prediction (SPRP) algorithm [9] (Section 3.2.4), consider the dual-band bandpass filter [29] shown in

Fig. 3.12. The design parameters are $\boldsymbol{x} = [L_1\ L_2\ S_1\ S_2\ S_3\ d\ g\ W]^T$ mm. The fine model is simulated in Sonnet ***em*** [27]. The design specifications are $|S_{21}| \geq -3$ dB for 0.85 GHz $\leq f \leq$ 0.95 GHz and 1.75 GHz $\leq f \leq$ 1.85 GHz, and $|S_{21}| \leq -20$ dB for 0.5 GHz $\leq f \leq$ 0.7 GHz, 1.1 GHz $\leq f \leq$ 1.6 GHz and 2.0 GHz $\leq f \leq$ 2.2 GHz. The coarse model is implemented in Agilent ADS [24] (Fig. 3.13). The initial design is $\boldsymbol{x}^{(0)} = [16.14\ 17.28\ 1.16\ 0.38\ 1.18\ 0.98\ 0.98\ 0.20]^T$ mm (the optimal solution of $\boldsymbol{R}_c$). The following characteristic points are selected to set up the SPRP surrogate model [9]: four points for which $|S_{21}| = -20$ dB, four points with $|S_{21}| = -5$ dB, as well as 6 additional points located between –5 dB points. For the purpose of optimization, the coarse model was enhanced by tuning the dielectric constants and the substrate heights of the microstrip models corresponding to the design variables L_1, L_2, d and g (original values of ε_r and H were 10.2 and 0.635 mm, respectively).

Figure 3.13 shows the initial fine model response as well as the fine model response at the design obtained using the stand-alone SPRP. Table 3.3 shows the optimization results. Two variants of the SPRP algorithm were considered [9]:

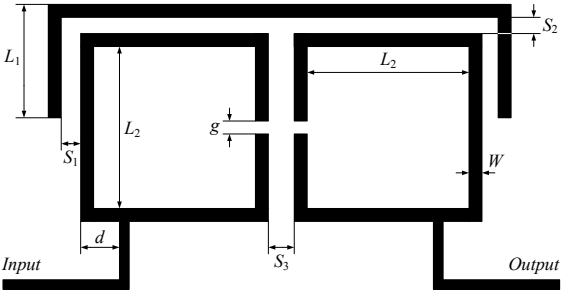

Fig. 3.12 Dual-band bandpass filter: geometry [29].

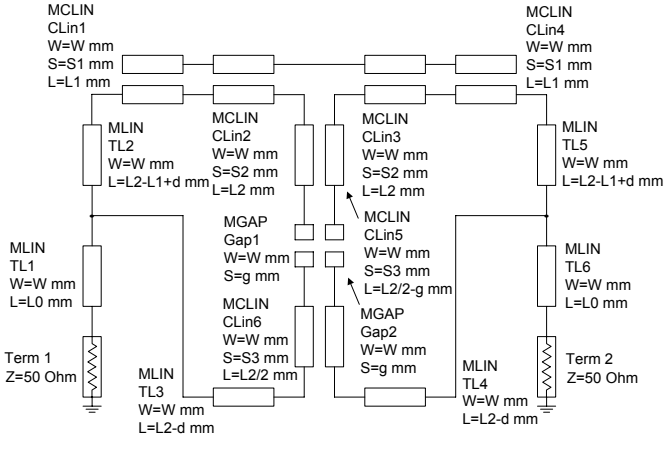

Fig. 3.13 Dual-band bandpass filter: coarse model (Agilent ADS).

Table 3.3 Optimization Results for Dual-Band Bandpass Filter

Algorithm	Final Specification Error [dB]	Fine Model Runs[1] [times]
SPRP	–2.0[3]	3
SPRP + input SM[2]	–1.9[4]	2

[1] Excludes the fine model evaluation at the starting point.
[2] Surrogate model is $\boldsymbol{R}_s^{(i)}(\boldsymbol{x}) = \boldsymbol{R}_c(\boldsymbol{x} + \boldsymbol{c}^{(i)})$; $\boldsymbol{c}^{(i)}$ is found using parameter extraction [9].
[3] Design specifications satisfied after the first iteration (spec. error –1.2 dB).
[4] Design specifications satisfied after the first iteration (spec. error –1.0 dB).

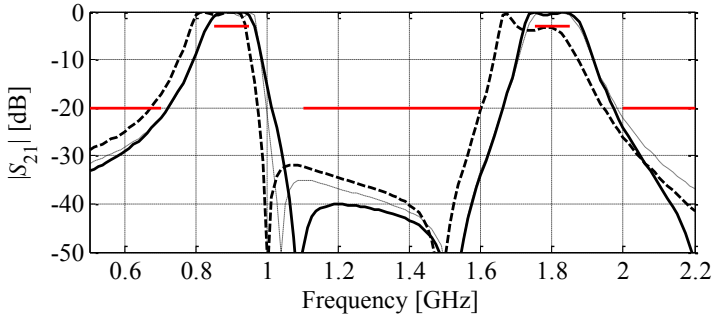

Fig. 3.14 Dual-band bandpass filter: fine model (dashed line) and coarse model (thin dashed line) response at $\boldsymbol{x}^{(0)}$, and the optimized fine model response (solid line) at the design obtained using SPRP.

stand-alone and combined with input SM. Note a very small number of fine model evaluations necessary to yield the optimized design.

3.4 Surrogate-Based Design Optimization of Antennas

Building a surrogate model may not be straightforward for certain types of microwave devices since reliable circuit equivalents, as those used in the previous section for planar microwave filters, may not be available for many types of antennas, e.g., ultrawide band (UWB) antennas, Yagi-type of antennas, or dielectric resonator antennas. Often, the only way to create a surrogate model is to use a coarsely-discretized full-wave EM model which is evaluated using the same EM solver as the one used for the high-fidelity model. However, coarsely-discretized EM simulation is still relatively expensive so that typically only a limited number of such simulations can be afforded. One way to deal with this situation is to generate smooth and computationally inexpensive surrogate by approximating sampled coarse-discretization EM data. The surrogate created this way can be then used in the space mapping optimization process. Another possibility is to exploits techniques that do not require excessive number of coarse-discretization EM simulations. Two of such methods—adaptive design specifications and multi-fidelity optimization algorithm—are also demonstrated in this chapter for antenna design.

3.4.1 Design of UWB Antipodal Vivaldi Antenna Using Coarsely-Discretized EM Models, Kriging and Space Mapping

The example considered here, a UWB antipodal Vivaldi antenna [30] of Fig. 3.15, shows how to combine functional and physical models to build a surrogate. Design variables are $\boldsymbol{x} = [a_1\ a_2\ b_1\ b_3\ h_1\ h_2\ d_1]^T$. The profile of the antipodal metal fins is with arks of ellipses; for the upper fin they are: *BC*, *DE*, and *DB*. The point *A* is the center of two ellipses with the arks of *BC* and *DE,* and the semiaxes of a_1 and b_1 and a_2 and b_2, respectively. The point *F* is the center of the ellipse with the semiaxes of a_3 and b_3. Note that here $a_3 = (a_2 - a_1)/2$, $b_2 = b_1 + w_s$, and $d_2 = d_1$. Other parameters are fixed: $w_s = 2.15$, $w_1 = 12.9$, and $h_3 = 5$ (all in mm). Antenna metallization is with 0.05 mm copper. The fins are interfaced with the microstrip input (width of the ground of w_1) through the linear taper of length h_2. Rogers RT5880 (0.787 mm thick) is for the substrate of finite extends, and dielectric losses are maximal at 10 GHz.

The design specifications for reflection are $|S_{11}| \leq -10$ dB for 3.1 GHz to 10.6 GHz. Total lateral and longitudinal dimensions are constrained by 100 mm and 200 mm, respectively. The antenna models include an edge mount SMA connector (AEP part number: 9650-1113-014) [31] and its hex nut since their presence, as it was seen from numerical experiments, can affect the radiation pattern, e.g., tilt the main beam from the end-fire direction, change the gain in the back direction, etc. The connector pin extends 0.5 mm from the flange over the microstrip signal trace. The upper connector tips, the lower connector tips, and the microstrip ground are connected with a pair of vias (1 mm in diameter) going through the substrate.

The mismatch level of the connector-to-input microstrip junction itself is below −28 dB in the bandwidth of interest. The antenna models are excited through the 50 ohm coaxial port which is in the SMA connector.

The initial design is $\boldsymbol{x}^{in} = [30\ 50\ 10\ 10\ 100\ 20\ 2]^T$ mm. The high-fidelity antenna model is evaluated with the CST MWS transient solver [3] (8,954,244 mesh cells at $\boldsymbol{x}^{in}$, simulation time 1h 45 min).

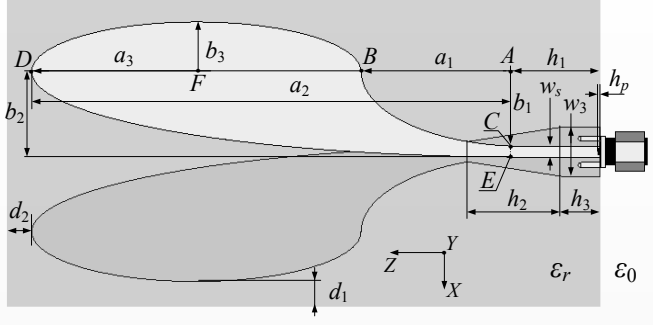

Fig. 3.15 Vivaldi antenna: top view, substrate shown transparent.

Here, a suitable equivalent-circuit coarse model is not available to apply optimization using space mapping. Instead, a coarse-discretization CST model $\boldsymbol{R}_{cd}$ (1,039,008 mesh cells at $\boldsymbol{x}^{in}$, evaluation time 6 minutes) is used. $\boldsymbol{R}_{cd}$ is still computationally too expensive to be used directly as a coarse model, therefore, a coarse model $\boldsymbol{R}_c$ is created in the neighbourhood of the starting point (here, the approximate optimum of $\boldsymbol{R}_{cd}$), using kriging interpolation [5] of the $\boldsymbol{R}_{cd}$ data. The procedure is as follows.

1. Allocate N base designs, $X_B = \{\boldsymbol{x}^1, \ldots, \boldsymbol{x}^N\}$, using Latin Hypercube Sampling [32];
2. Evaluate $\boldsymbol{R}_{cd}$ at each design $\boldsymbol{x}^j$, $j = 1, 2, \ldots, N$;
3. Build $\boldsymbol{R}_c$ as a kriging interpolation of data pairs $\{(\boldsymbol{x}^j, \boldsymbol{R}_{cd}(\boldsymbol{x}^j))\}_{j = 1,\ldots,N}$.

The coarse model created this way is computationally cheap, easy to optimize, and yet retains the features of a physically-based model. The starting point for space mapping optimization, $\boldsymbol{x}^{(0)} = [37.57\ 32.85\ 25.75\ 53.34\ 122.55\ 32.31\ 1.129]^T$ mm, is the approximate optimum of $\boldsymbol{R}_{cd}$. The kriging coarse model $\boldsymbol{R}_c$ is set up in the vicinity of $\boldsymbol{x}^{(0)}$ using $N = 100$ base points.

Figure 3.16 shows the fine model reflection response at the initial design as well as that of the fine and coarse-discretization model $\boldsymbol{R}_{cd}$ at $\boldsymbol{x}^{(0)}$. The final design, $\boldsymbol{x}^{(2)}=[37.66\ 33.16\ 25.21\ 53.22\ 122.50\ 33.06\ 1.012]^T$ mm, is obtained after two space mapping iterations (Fig. 3.17). The surrogate model used by the optimization algorithm exploited input and output space mapping of the form $\boldsymbol{R}_s(x) = \boldsymbol{R}_c(\boldsymbol{x} + \boldsymbol{c}) + \boldsymbol{d}$ [7]. Optimization costs are summarized in Table 3.4. The total design time corresponds to about 16 evaluations of the fine model. It should be noted that the design improvement between $\boldsymbol{x}^{(0)}$ and $\boldsymbol{x}^{(2)}$ is somehow limited, which is because of a limited accuracy of the coarse model as shown in Fig. 3.16. The far-field response of the final design at selected frequencies is shown in Fig. 3.18.

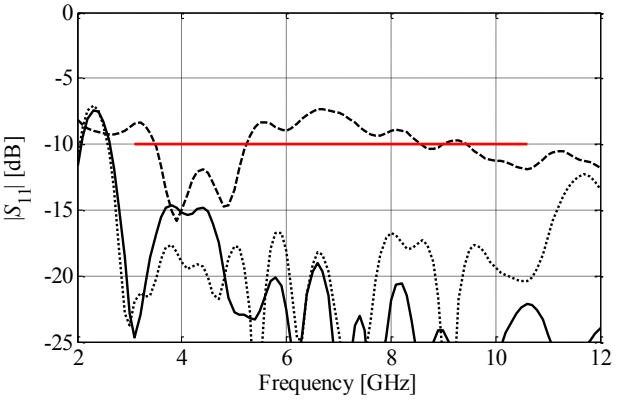

Fig. 3.16 Vivaldi antenna, $|S_{11}|$ versus frequency: Fine model $\boldsymbol{R}_f$ at the initial design (- - -), optimized coarse-discretization model $\boldsymbol{R}_{cd}$ (· · ·), and $\boldsymbol{R}_f$ at the optimum of $\boldsymbol{R}_{cd}$ (—).

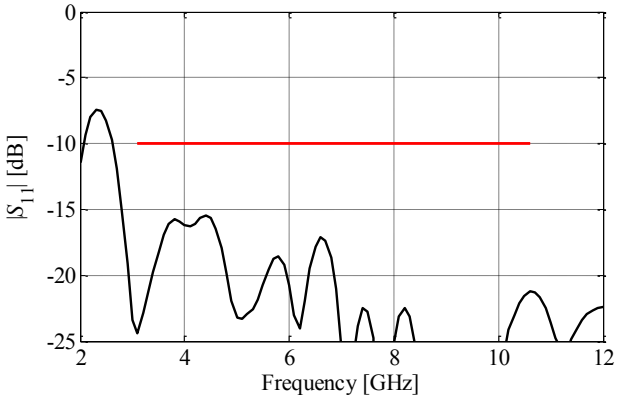

Fig. 3.17 Vivaldi antenna, $|S_{11}|$ versus frequency: $\boldsymbol{R}_f$ at the final design.

Table 3.4 UWB Vivaldi antenna: optimization cost

Algorithm Component	Number of Model Evaluations	CPU Time	
		Absolute	Relative to $\boldsymbol{R}_f$
Optimization of $\boldsymbol{R}_{cd}$	$135 \times \boldsymbol{R}_{cd}$	13.5 hours	7.7
Setting up $\boldsymbol{R}_c$	$100 \times \boldsymbol{R}_{cd}$	10.0 hours	5.7
Evaluation of $\boldsymbol{R}_f$	$3 \times \boldsymbol{R}_f$	5.3 hours	3.0
Total cost	N/A	28.8 hours	16.4

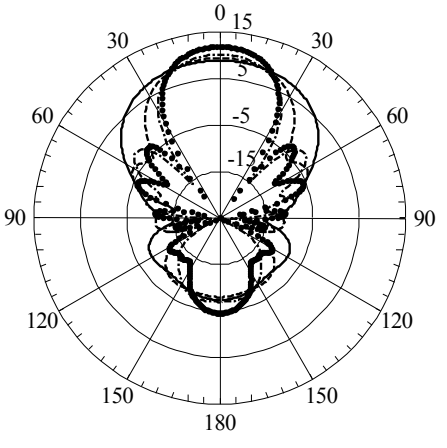

Fig. 3.18 Gain [dBi] of the Vivaldi antenna, x-pol. component: pattern cut in YOZ plane at 4 GHz (—), 6 GHz (- - -), 8 GHz (- · - · -), and 10 GHz (•••). 90^0 on the left, 0^0, and 90^0 on the right are for Y, Z, and $-Y$ directions, respectively.

3.4.2 Design of Planar Yagi Antenna Using Adaptive Design Specifications

Performance of the adaptive design specifications methodology [11] can be demonstrated with design optimization of a planar Yagi antenna for the 2.4-2.5 GHz band [33]. Optimization of planar Yagi antennas on finite substrate is a challenging task due to the finite substrate and proximity of the feeding circuitry to the radiators both introducing additional degrees of freedom to the design as well as complicate the use of methods developed for Yagi aerials [34, 35] and permits a limited use of existing design techniques [36].

Design geometry. The considered Yagi antenna comprises three directors, one driving element of a modified shape consisting of partially overlapping strips, and the feeding microstrip ground plane serving also as the reflector. The presented antenna can be viewed as a planar realization of the five-element Yagi. An outline of the antenna is given with Fig. 3.19. The antenna components are defined on a single layer of 0.025" thick Rogers RT6010 substrate which has extends of 100 mm × 160 mm. The ground extend is 100 mm × 40 mm. The input 50 ohm microstrip is to be interfaced to the terminals of the driving element through a section of the parallel strip transmission line in a way that provides the balanced input to the antenna. The antenna model is defined with CST MWS, discretized with subgrids, and simulated using the CST transient solver.

Design objectives. Maximum directivity of the principal polarization (E-field is parallel to XOZ plane) in the 2.4-2.5 GHz band is chosen as the main objective. The following antenna figures are treated as constraints (also in the 2.4-2.5 GHz band): the side lobe level relative to maximum (SLL < –10 dB), front-to-back ratio (FBR < –12 dB), direction of maximal radiation θ_m (elevation angle from the

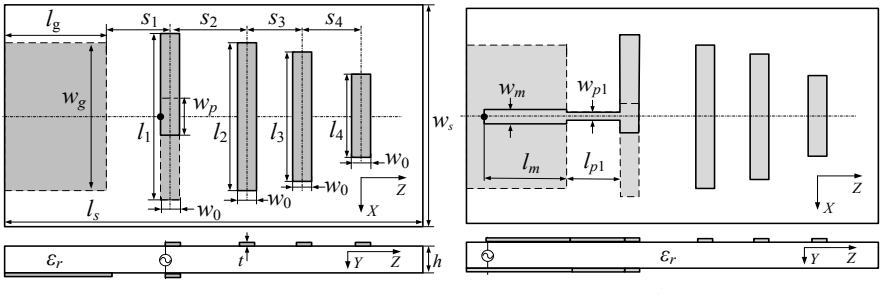

Fig. 3.19 Printed quasi-Yagi antenna: (a) the model used at the optimization stage of design (no feeding section), (b) the model updated with a feeding section starting from the 50 ohm microstrip. Source impedance is not shown at the diagrams. For simplicity, the feeding section at the panel (b) is shown as a simple two section structure: 50 ohm microstrip (dimensions l_m and w_m) and parallel strips (dimensions l_{p1} and w_{p1}). Detailed geometry of the optimized feeding section is given with Fig. 3.21(a).

Z axis, $|\theta_m| < 1^o$). The antenna should be interfaced to the 50 ohm environment so that $|S_{11}| < -10$ dB in the 2.4-2.5 GHz band.

Design stages. As the input impedance of Yagi antennas is typically sensitive to variations of antenna dimensions [36], and since its value is not available prior to simulation while it is needed to define the feeding part of the antenna, the design optimization proceeds in two major steps as follows: First, the antenna is optimized for maximal directivity subject to the constraints on SLL, FBR, and θ_m. At this step the excitation is applied directly at the driving element's terminals (Fig. 3.19(a)). Design optimization procedure is based on surrogate-based optimization and involves optimization of a coarse-discretization antenna model. Having the optimal design, the feed interfacing the 50 ohm input and the driving element terminals, is designed.

Optimization methodology. Optimization of the coarse-discretization antenna model is carried out much faster. However, the coarse-discretization model is also less accurate: the figures of interest (e.g., directivity, SLL, FBR) are shifted in frequency with respect to those of the high-fidelity model. The frequency relationship between the two models using characteristic points (e.g., local maxima, points of corresponding response levels) is captured as shown in Fig. 3.20. Using this relationship, the original frequency band of interest is mapped into the corresponding band that is used in the optimization of the coarse-discretization model. This procedure, i.e., mapping of the frequency band, optimization of the coarse-discretization model and evaluation of the high-fidelity model is performed a few times as the frequency dependence between the models' responses may change from one design to another. The high-fidelity model is only evaluated a few times for verification purposes and to set up a new mapping.

Results. The design variables when optimizing the antenna for maximal directivity are $\boldsymbol{x} = [l_1\ l_2\ l_3\ l_4\ s_1\ s_2\ s_3\ s_4\ w_0\ w_p]^T$ (Fig. 3.19(a)). Other parameters are fixed: l_s=160, w_s = 100, l_g = 40, w_g = 100, and h = 0.635 (all in mm). The initial design is $\boldsymbol{x}^{(0)}$ = [40.42 35.7 31.5 27.3 17.85 22.05 22.05 22.05 2.35 1.5]^T. Simulation time of the coarse-discretization model (51,580 cells at $\boldsymbol{x}^{(0)}$) is about 6 minutes, and it is about 2 hours for the original, high-fidelity model (1,096,980 cells at $\boldsymbol{x}^{(0)}$). The optimum is found at $\boldsymbol{x}^*$ = [40.87 37.31 34.33 29.80 17.35 22.55 23.05 24.55 1.55 2.13]^T.

Based on the optimum $\boldsymbol{x}^*$ and the antenna impedance at the driving element terminals Z_t (Fig. 3.19(a)), a feed is designed (Fig. 3.21) using analytical formulas with a microstrip (l_m = 35 mm, w_m = 0.586 mm) and parallel strips ($l_{p1} = s_1 - w_0/2$, w_{p1} = 0.36 mm). The updated antenna model is then simulated. Its reflection does not meet the design specifications for frequency over 2.484 GHz. Therefore, the feed is redesigned with geometry of Fig. 3.21(a) through optimization of its full-wave model and a schematic of Fig. 3.21(b). Dimensions of the simple feed are used as an initial guess. Optimal feed dimensions are found to be $[w_{p1}\ w_{p2}\ w_{p3}\ l_{p1}\ l_{p2}]^T$ = [0.428 0.275 0.245 0.575 8.08]^T. The updated antenna model is then simulated, and responses are shown in Figs. 3.22 through 25 and Table 3.5. Table 3.6 shows the computational cost of the optimization process, which corresponds to only 19 full-wave antenna simulations.

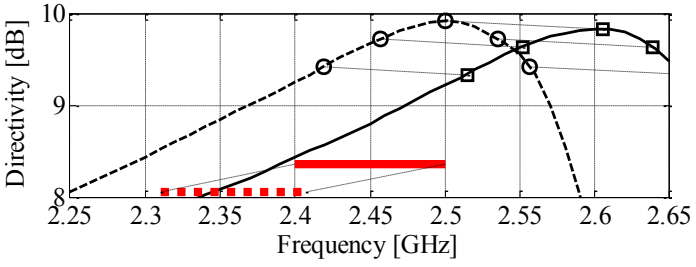

Fig. 3.20 Directivity versus frequency for the antenna structure (solid line) and its coarse-discretization model (dashed line). Characteristic points (squares and circles) are used to establish a frequency relationship between the two responses and to map the original frequency band of interest (2.4 to 2.5 GHz, thick solid line) into the corresponding band used in the coarse-discretization model optimization (thick dashed line).

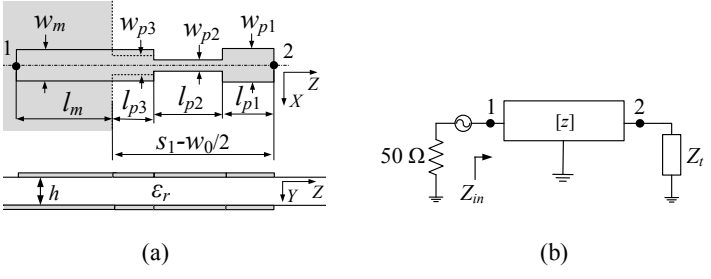

Fig. 3.21 A feed interfacing the 50 ohm input and the driving elements: (a) geometry of its full-wave model; (b) implemented schematic.

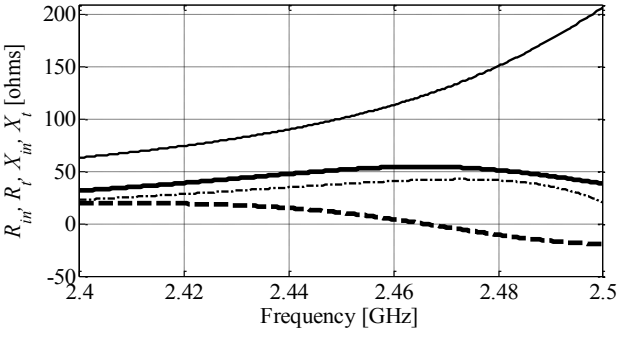

Fig. 3.22 Antenna impedance: resistance R_{in} (thick solid) and reactance X_{in} (thick dash) at the antenna input (Fig. 3.19(b)); R_t (solid) and X_t (dash-dot) at the driving element terminals (Fig. 3.19(a)).

Table 3.5 Printed Yagi antenna: performance summary

Figure	Value
Directivity, maximum*	10 dBi
Directivity, end fire maximum*	9.85 dBi
IEEE gain, end fire maximum*	9.49 dBi
Radiation efficiency, minimum*	92 %
Front to back ratio (FBR), minimum*	15.5 dB
Side lobe level (SLL), maximum*	-10.2 dB
End-fire polarization purity, minimum*	40 dB
3 dB beamwidth at 2.45 GHz	E-plane: 59°, H-plane: 74°
Relative bandwidth ($\|S_{11}\| < -10$ dB)	4.4 %
Input impedance at resonance (2.466 GHz)	54.6 ohms

* maximum/minimum over 2.4 GHz to 2.5 GHz

Table 3.6 Printed Yagi antenna: optimization cost summary

Algorithm Component	# of Model Evaluations	Absolute Time	Relative Time[3]
Coarse-discretization model optimization[1]	316	32 h	16
High-fidelity antenna simulation[2]	3	6 h	3
Total optimization time[4]	-	38 h	19

[1] Total number of evaluations (coarse-discretization model is optimized once per iteration, two iterations were performed in total).
[2] Evaluation at the initial design and after each iteration.
[3] Equivalent number of high-fidelity antenna simulations.
[4] Does not include the time necessary to design the antenna feed, which is negligible compared to the optimization time of the antenna itself.

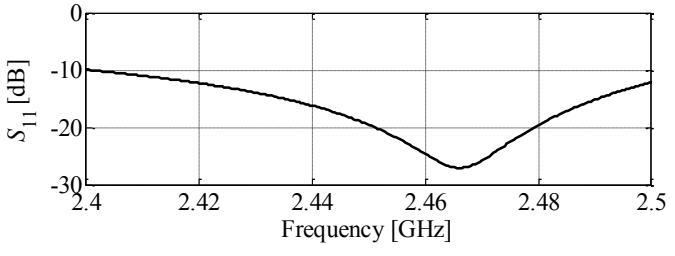

Fig. 3.23 Reflection from the input of the Yagi antenna.

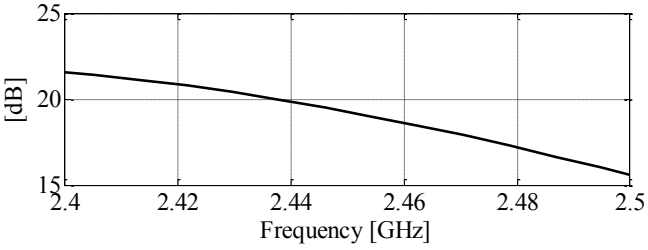

Fig. 3.24 Front-to-back ratio.

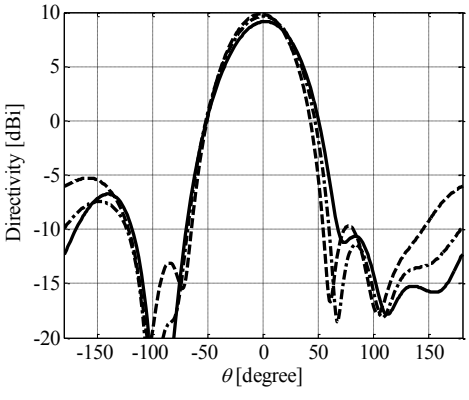

(a)

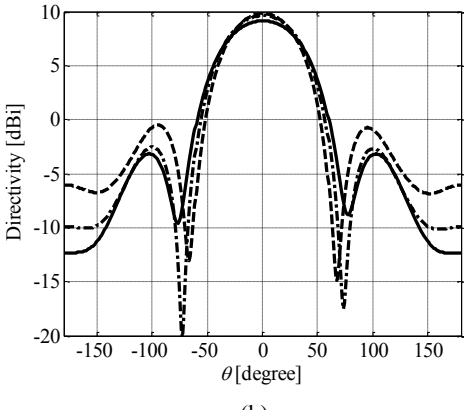

(b)

Fig. 3.25 Directivity pattern at 2.4 GHz (solid), 2.45 GHz (dash-dot), and 2.5 GHz (dash): (a) co-pol. in the E-plane (XOZ); (b) ×-pol. in the H-plane (YOZ).

3.4.3 Multi-fidelity Design of Microstrip Broadband Antenna

Application of the multi-fidelity optimization algorithm [10] is demonstrated below using the broadband antenna [37] shown in Fig. 3.26. Here, $\boldsymbol{x} = [l_1\ l_2\ l_3\ l_4\ w_2\ w_3\ d_1\ s]^T$ are the design variables. Multilayer substrate is $l_s \times l_s$ (l_s=30 mm). The stack (from bottom-to-top) is: ground, RO4003, signal trace, RO3006 with a through via (trace-to-patch), the driven patch, RO4003, and four patches. Feeding is with 50 ohm SMA connector.

The design objective is $|S_{11}| \leq -10$ dB for 3.1 GHz to 10.6 GHz. IEEE gain not less than 5 dB for the zero elevation angle over band is an optimization constrain. The initial design is $\boldsymbol{x}^{(0)} = [15\ 15\ 15\ 15\ 20\ -4\ 2\ 2]^T$ mm. Two coarse-discretization models are used: $\boldsymbol{R}_{c.1}$ (122,713 mesh cells at $\boldsymbol{x}^{(0)}$) and $\boldsymbol{R}_{c.2}$ (777,888 mesh cells). The evaluation times for $\boldsymbol{R}_{c.1}$, $\boldsymbol{R}_{c.2}$ and $\boldsymbol{R}_f$ (2,334,312 mesh cells) are 3 min, 18 min and 160 min at $\boldsymbol{x}^{(0)}$, respectively. Figure 3.27(a) shows the responses of $\boldsymbol{R}_{c.1}$ at $\boldsymbol{x}^{(0)}$ and at its optimal design $\boldsymbol{x}^{(1)}$. Figure 3.27(b) shows the responses of $\boldsymbol{R}_{c.2}$ at $\boldsymbol{x}^{(1)}$ and at its optimized design $\boldsymbol{x}^{(2)}$. Figure 3.26(c) shows the responses of $\boldsymbol{R}_f$ at $\boldsymbol{x}^{(0)}$, at $\boldsymbol{x}^{(2)}$ and at the refined design $\boldsymbol{x}^* = [14.87\ 13.95\ 15.4\ 13.13\ 20.87\ -5.90\ 2.88\ 0.68]^T$ mm ($|S_{11}| \leq -11.5$ dB for 3.1 GHz to 4.8 GHz) obtained in two iterations of the refinement step [10], see also Section 3.2.5,

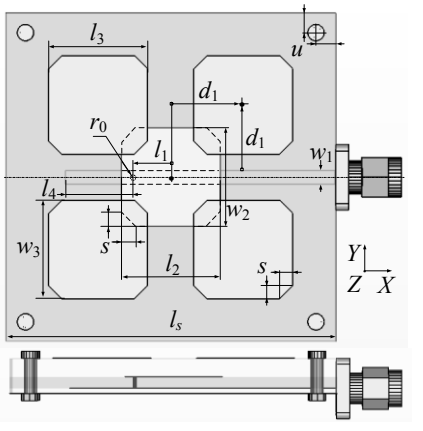

Fig. 3.26 Microstrip broadband antenna: top/side views, substrates shown transparent.

Table 3.7 Microstrip broadband antenna: design cost

Design Step	Model Evaluations	Computational Cost	
		Absolute [hours]	Relative to $\boldsymbol{R}_f$
Optimization of $\boldsymbol{R}_{c.1}$	$125 \times \boldsymbol{R}_{c.1}$	6.3	2.6
Optimization of $\boldsymbol{R}_{c.2}$	$48 \times \boldsymbol{R}_{c.2}$	14.4	5.4
Setup of model $\boldsymbol{q}$	$17 \times \boldsymbol{R}_{c.2}$	5.1	1.9
Evaluation of $\boldsymbol{R}_f$	$2 \times \boldsymbol{R}_f$	5.3	2.0
Total design time	N/A	31.1	11.9

* Excludes $\boldsymbol{R}_f$ evaluation at the initial design.

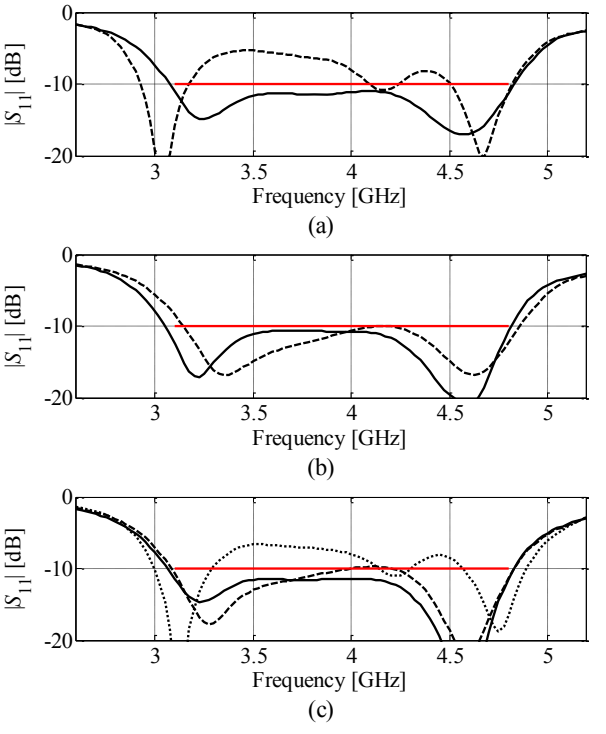

Fig. 3.27 Microstrip broadband antenna: (a) responses of the coarse-discretization model $\boldsymbol{R}_{c.1}$ at the initial design $\boldsymbol{x}^{(0)}$ (- - -) and at the optimized design $\boldsymbol{x}^{(1)}$ (—); (b) responses of the coarse-discretization model $\boldsymbol{R}_{c.2}$ at $\boldsymbol{x}^{(1)}$ (- - -) and at its optimized design $\boldsymbol{x}^{(2)}$ (—); (c) responses of the high-fidelity model $\boldsymbol{R}_f$ at $\boldsymbol{x}^{(0)}$ (····), at $\boldsymbol{x}^{(2)}$ (- - -) and at the refined final design $\boldsymbol{x}^*$ (—).

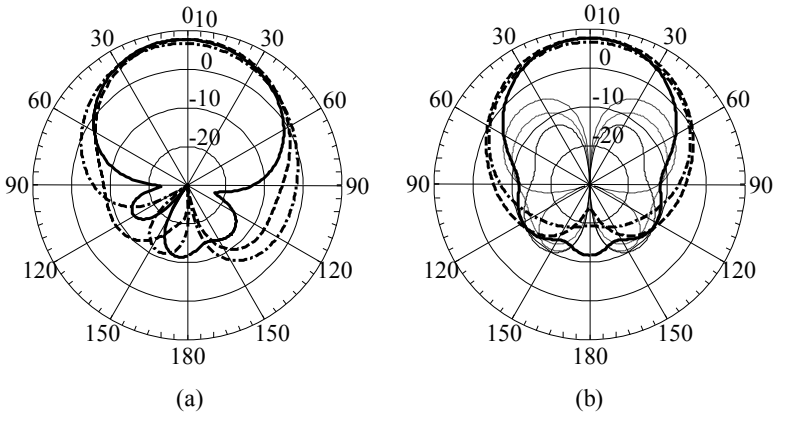

Fig. 3.28 Microstrip antenna, gain [dBi] of the final design at 3.5 GHz (· − ·), 4.0 GHz (− −), and 4.5 GHz (—): (a) co-pol. in the *E*-plane (*XOZ*), and connector is at 90^0 on the right; (b) x-pol., primary, (thick lines) and co-pol. (thin lines) in the *H*-plane (*YOZ*).

eq. (3.13). The design cost (Table 3.7) corresponds to about 12 runs of the high-fidelity model $\boldsymbol{R}_f$. Antenna gain at the final design is shown in Fig. 3.28.

3.5 Surrogate-Based Design Optimization of Microwave Transitions

Design of low-loss broad-band transitions interfacing different type of transmission lines at microwave frequencies usually involves full-wave EM simulation to accurately describe the transition responses [38, 39]. Circuit models and analytical formulas, when available, can only be used to get initial designs which should be verified and tuned for required design requirements. Typically, reliable circuit models are either unavailable or require significant amount of development and validation effort. Moreover, additions or modifications introduced in the transition geometry may invalidate existing models, which leads to repeating the model development procedure. On the other hand, optimization techniques exploiting surrogates [40], including those based on coarsely-discretized EM models, may substantially reduce the computational complexity of the conventional optimization methods and, at the same time, be applied to modified/improved geometries without extra effort.

Two examples are presented in this section. The first one illustrates the multi-fidelity design optimization technique to improve performance of a coplanar waveguide-to-microstrip transition based on EM coupling. The second example demonstrates the use of the adaptive design specifications method for design of coplanar waveguide-to-substrate integrated waveguide transition. In both cases the use of coarsely-discretized EM models is essential, since no accurate circuit equivalents are available for the considered structures.

3.5.1 Multi-fidelity Design of Microstrip-to-Coplanar Waveguide Transition

Here, the multi-fidelity optimization algorithm [10] is applied to design optimization of a microstrip-to-CPW transition [41]. The methodology exploits sequential optimization of coarse-discretization EM models. The optimal design of the current model is used as an initial design for the finer-discretization one. The final design is then refined using a polynomial-based approximation model of the responses obtained from the coarse-discretization simulations. The design process is computationally efficient because the optimization burden is shifted to the coarse-discretization models.

Two frequency bands with the center frequencies f_c of 5 GHz and 10 GHz are of interest for this transition [41] (Fig. 3.29). The port-to-port distance is 20 mm. The transition geometry and the input transmission lines (TLs) are on 0.635 mm thick RT6010 substrate. Metallization (5.7e8 S/m) is 0.0254 mm thick. Dimensions of the input TLs are the following: W_m=0.6, W_c=0.8, and s_c=0.3 (all in mm). The ground plane is common to the CPW and microstrip and it is modelled of infinite lateral extend. The low frequency TL impedances are about 50 ohms each. All models are simulated using the CST MWS transient solver.

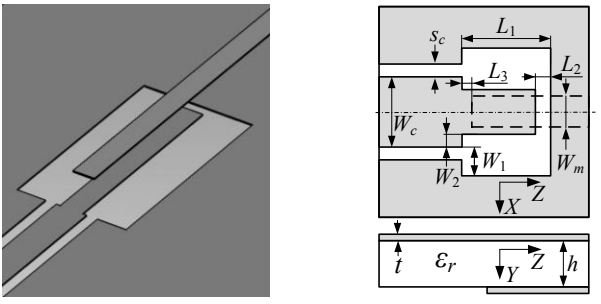

Fig. 3.29 Coplanar waveguide-to-microstrip transition with EM coupling [41]: (a) 3D view, substrate shown transparent; (b) layout views.

In this example the ground plane is modelled to be of infinite lateral extend. The design objective is the 50% symmetrical bandwidth at the –20 dB level for both $|S_{11}|$ and $|S_{22}|$. The design variables are $\boldsymbol{x} = [L_1\ W_1\ W_2\ L_2\ L_3]^T$ mm. Designs start from $\boldsymbol{x}^{(0)} = [L^{(0)}_1\ 0.8\ 0\ 0.3\ 0]^T$, where $L^{(0)}_1 = 6$ and 3 for designs of 5 GHz and 10 GHz, respectively. For this example one again uses two coarse-discretization models $\boldsymbol{R}_{c.1}$ and $\boldsymbol{R}_{c.2}$ with the following evaluation times: 60s and 100s (5 GHz) and 71 s and 106 s (10 GHz). The fine model evaluation time is 17 min (5 GHz) and 26 min (10 GHz).

The optimal designs are found to be $\boldsymbol{x}^* = [6.200\ 1.105\ \ 0.113\ 0.319\ –0.033]^T$ for 5 GHz and $[2.877\ 1.017\ 0.038\ \ 0.287\ –0.090]^T$ for 10 GHz. Both final designs meet the specifications completely, which is shown in Fig. 3.30. Figure 3.31 shows the transmission responses $|S_{21}|$ versus frequency at the initial and final designs. Significant improvement in reflection and transmission responses (in level and bandwidth) is achieved: the bandwidth was extended to 53% from initial 0% for the 5 GHz design and to 51% from initial 20% for the 10 GHz design. Design cost are 9.3 evaluations of the fine model for the 5 GHz design and 7.0 evaluations of the fine model for the 10 GHz design (see Table 3.8 for details).

As a comparison with "classical" simulation-driven design, the transition for f_c = 10 GHz has been also designed through direct optimization of the fine model using the pattern search algorithm [42]. The final design obtained this way is almost as good as that produced by the multi-fidelity technique (50% bandwidth), however, the design cost is almost 18 times higher (124 evaluations of $\boldsymbol{R}_f$ versus about 7 for the multi-fidelity algorithm).

The reduced quadratic model [10], see also Section 3.2.5, eqs. (3.11)-(3.12), is also utilized to perform sensitivity analysis of the final designs. For this purpose, however, the quadratic model is set up using the high-fidelity model data. Because sensitivity analysis is performed assuming relatively small deviations around the optimized design (0.0125 and 0.025 mm for geometry variables), the accuracy of the quadratic model is sufficiently good with respect to $\boldsymbol{R}_f$. Results of the sensitivity analysis are shown in Fig. 3.32.

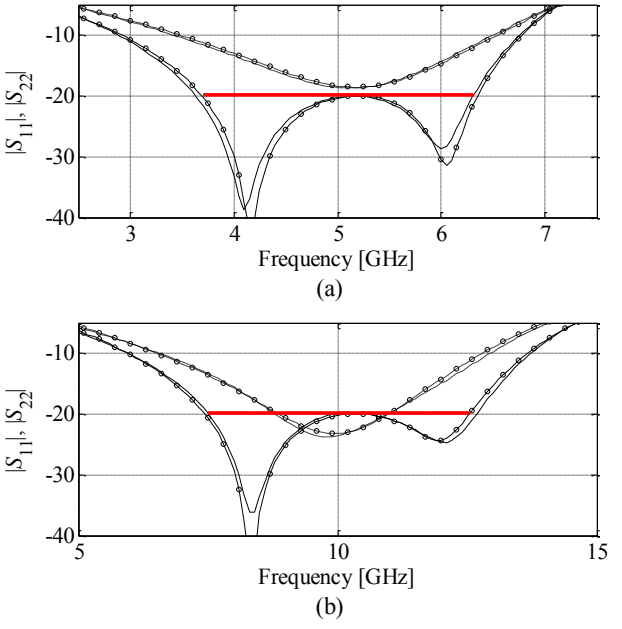

Fig. 3.30 Transition through coupling: fine model responses at initial (dashed line) and final design (solid line) for (a) f_c = 5 GHz, and (b) f_c = 10 GHz; –20 dB bandwidth at the final design marked with horizontal line.

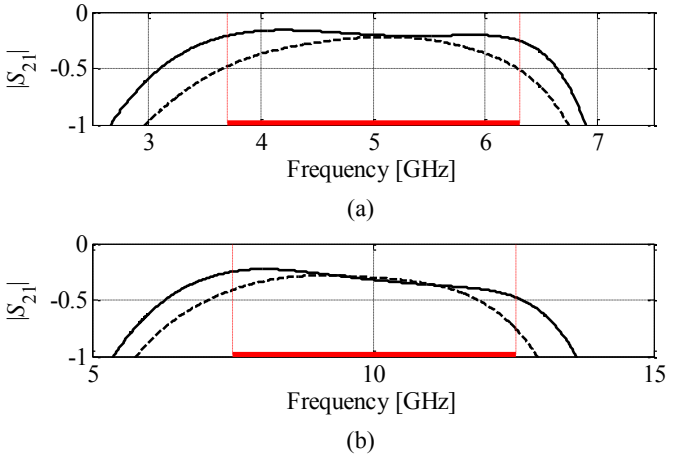

Fig. 3.31 Transition through coupling: transmission response at the initial (dashed line) and the final design (solid line) for (a) f_c = 5 GHz and (b) f_c = 10 GHz; –20 dB bandwidth at the final design marked with horizontal line.

Table 3.8 CPW-microstrip transition: design cost

Center frequency	Design Procedure Component	Number of Model Evaluations	Evaluation Time	
			Absolute [min]	Relative to $\boldsymbol{R}_f$
5 GHz	Optimization of $\boldsymbol{R}_{c.1}$	62	62	3.6
	Optimization of $\boldsymbol{R}_{c.2}$	27	45	2.6
	Setup of model $\boldsymbol{q}$	11 ($\boldsymbol{R}_{c.2}$)	18	1.1
	Evaluation of $\boldsymbol{R}_f$	2	34	2.0
	Total design time	N/A	**159**	**9.3**
10 GHz	Optimization of $\boldsymbol{R}_{c.1}$	54	64	2.5
	Optimization of $\boldsymbol{R}_{c.2}$	26	46	1.8
	Setup of model $\boldsymbol{q}$	11 ($\boldsymbol{R}_{c.2}$)	19	0.7
	Evaluation of $\boldsymbol{R}_f$	2	52	2.0
	Total design time	N/A	**181**	**7.0**

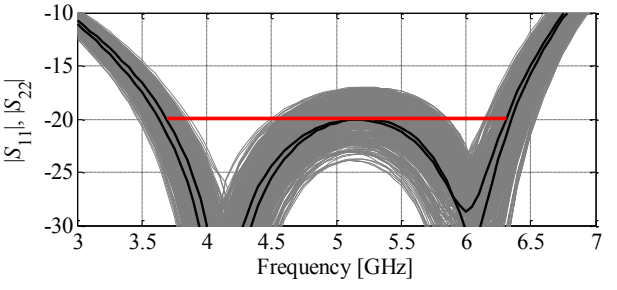

(a)

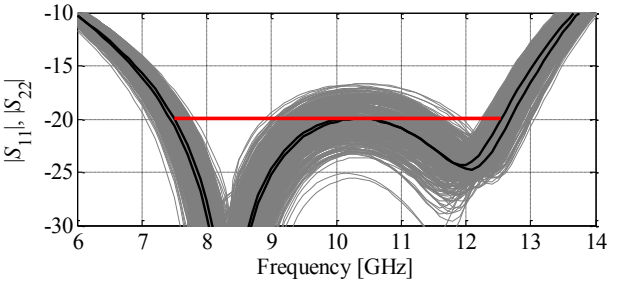

(b)

Fig. 3.32 Transition through coupling: sensitivity analysis using 200 random samples allocated in the neighbourhood of the optimized designs: (a) f_c = 5 GHz and (b) f_c = 10 GHz; – 20 dB bandwidth at the final design marked with horizontal line. The sensitivity analysis setup is described in the text. Thick solid lines denote transition responses at optimized designs. Thin lines represent the family of responses corresponding to random samples as described above.

3.5.2 Design of Coplanar Waveguide-to-Substrate Integrated Waveguide Transition

Substrate integrated circuits (SICs), and substrate integrated waveguides (SIWs) in particular, find application in modern microwave and millimeter wave engineering due to their capability of low cost realization of waveguide components as well as integration of different components all in the frame of planar technology [43]. One of the major tasks in SIC transition design is the adjustment of geometry parameters so that given design specifications are satisfied. For research in the computer aided design (CAD), this casts into a problem of developing straightforward and reliable procedures to tune geometries of SIC transitions for required performance in a given environment.

Increasing a useable bandwidth of conductor backed coplanar waveguide (CBCPW)-to-SIW transitions is targeted here. Metalized vias partially protruding into substrate in the transition region are used as tuning elements, and the surrogate-based optimization [7] is applied as a design tool. Adjustable metal screws and pins are classical tuning elements in hollow waveguides and cavities [44]; however, they are not used in SICs in the similar way since post-manufacturing adjustment of SICs is hardly possible, and finding optimal position, diameter, and protruding depth of vias represents a challenging task in the case of SIC. Design of SIC transitions can be conducted successfully by means of surrogate-based optimization [7], [45] and coarse-discretization electromagnetic models [46] with the transition dimensions considered as design optimization variables.

Examples include: (i) design optimization of a transition interfacing the conductor backed coplanar waveguide (CBCPW) to SIW without vias (not capable to satisfy the design specifications), and (ii) re-optimized transitions with metalized vias protruding into substrate in the transition region, which improves the usable bandwidth.

Geometry under design. Consider the planar transition interfacing a conductor backed coplanar waveguide (CBCPW) to a SIW shown in Fig. 3.33. The CBCPW, SIW, and transition are on the 3.175 mm RT5880 substrate. The CBCPW upper and lower grounds, the SIW top and bottom walls are of infinite lateral extend. All metal parts have conductivity of copper (5.8e7 S/m). Metallization of the CBCPW signal trace, CBCPW upper ground, and SIW top wall is with 1.5 oz copper (≈ 0.05 mm). Design specifications are $|S_{11}|$, $|S_{22}|$<= −20 dB for the *X*-band (here 8.2 GHz to 11.7 GHz).

The dimensions of the input CBCPW are: signal trace width w_0 = 2.25 mm; slot width s_0 = 0.2 mm; spacing between the rows of vias u_0 = 6.95 mm; spacing between vias in the row v_0 = 2 mm; via diameter d = 1 mm. The dimensions of the input SIW are: spacing between the rows of vias, u_2 = 15.95 mm; spacing between vias in the terminating rows v_1 = 1.5 mm; spacing between vias in the row v_2 = 2 mm; via diameter is the same as in the CBCPW (1 mm). The cutoff of the SIW's quasi TE_{10} dominant mode is at 6.55 GHz.

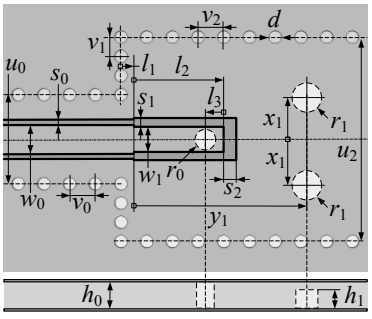

Fig. 3.33 CBCPW-to-SIW transition with two vias added: top and side views. The via walls are not shown on the side view. The dash-dot line shows the location of the symmetry plane (magnetic wall).

The transition comprises a CBCPW section, the probe connecting the CBCPW signal trace to the SIW bottom wall, and pairs of protruding vias. The length of the transition, i.e., $l_1 + l_2$ in the case without protruding vias, and $l_1 + y_1$ in the case of two protruding vias, is constrained to 20 mm (≈ 1.25 of u_2). Figure 3.2 gives a conceptual view of the transition with two extra vias. Via location, x_1, y_1, radius, r_1, and protruding depths, h_1, will be additional (to the dimensions of the CBCPW section) design variables. In the CAD models, the port-to-port distance is 55 mm of which 25 mm is for the SIW section. The SIW is excited through a 2.5 mm section of the equivalent rectangular waveguide [46]. The 50 ohm CBCPW waveguide port has a perfect metal periphery connecting the upper and lower CBCPW grounds. The extra vias protrude into the dielectric from the SIW bottom wall but they are not allowed to touch the SIW top wall.

Design process. The first step of the optimization process is to optimize the coarse-discretization EM model of the transition (low-fidelity model) using pattern search [42]. The design is further improved using adaptively adjusted design specifications technique [46, 47] which consists of the following two steps: (i) Modify the original design specifications to account for the discrepancy between the low- and high-fidelity models; (ii) Obtain a new design by optimizing the low-fidelity model with respect to the modified specifications.

In Step (i), the design specifications are modified so that the level of satisfying/violating the modified specifications by the low-fidelity model response corresponds to the satisfaction/violation levels of the original specifications by the high-fidelity model [46]. The low-fidelity model is then optimized in Step (ii) with respect to the modified specifications and the new design obtained this way is treated as an approximated solution to the original design problem (i.e., optimization of the high-fidelity model with respect to the original specifications). Steps (i) and (ii) can be repeated if necessary. Typically, a substantial design improvement is observed after the first iteration. Additional iterations may bring further enhancement as the discrepancy between the high- and low-fidelity models may change somehow

from one design to another. Figure 3.34 illustrates an iteration of this technique used for design of a CBCPW-to-SIW transition.

It should be noted that employing simulation-driven design based on low-fidelity models allows us to find optimal designs that might not be obtainable otherwise.

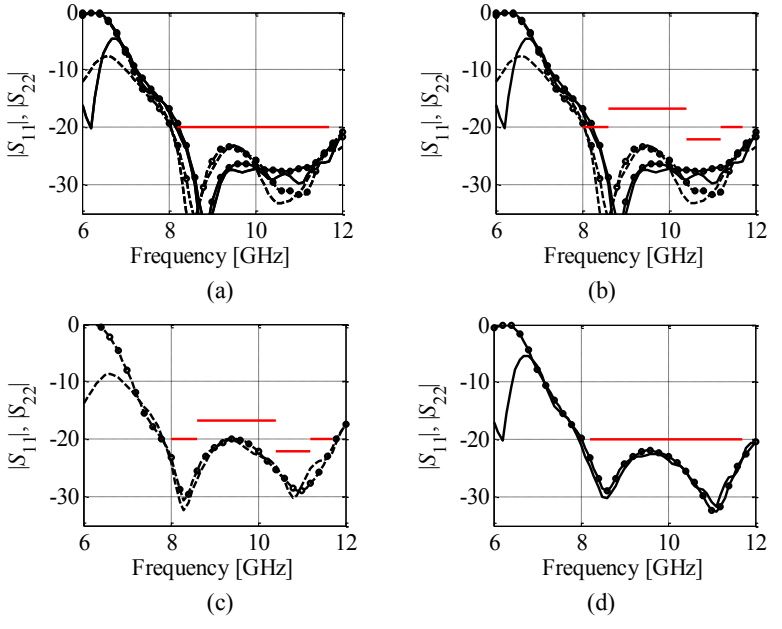

Fig. 3.34 Adaptively adjusted design specification technique applied to optimize CBCPW-to-SIW transitions. High- and low-fidelity model response denoted as solid and dashed lines, respectively. $|S_{22}|$ distinguished from $|S_{11}|$ using circles. Design specifications denoted by thick horizontal lines. (a) High- and low-fidelity model responses at the beginning of the iteration as well as original design specifications; (b) High- and low-fidelity model responses and modified design specifications that reflect the differences between the responses; (c) Low-fidelity model optimized to meet the modified specifications; (d) high-fidelity model at the low-fidelity model optimum shown versus original specifications.

Results. For the case without extra vias the design variables are $\boldsymbol{x}_{0in}=[l_1\ l_2\ l_3\ w_1\ s_1\ s_2\ r_0]^T$. The optimization procedure starts from $\boldsymbol{x}_{0in}=[1.0\ 7.0\ 0.75\ 2.0\ 0.4\ 1.0\ 0.75]^T$. The responses of the initial design are shown in Fig. 3.35 (a) and Fig 3.36(a). The optimal design is found to be $\boldsymbol{x}_{0opt}=[0.695\ 7.451\ 0.323\ 2.387\ 0.764\ 0.235\ 0.250]^T$, its responses are shown at Fig. 3.35(a) and Fig 3.36(a). The optimal design has the improved reflection and transmission responses compared to the initial one; however, it does not meet the design requirements. Therefore, additional vias are introduced (see Fig. 3.33) as tuning elements. The optimum design for the case of two protruding vias is shown in Table 3.9. The response corresponding to this design is shown in Fig. 3.35(b) and Fig 3.36 (b).

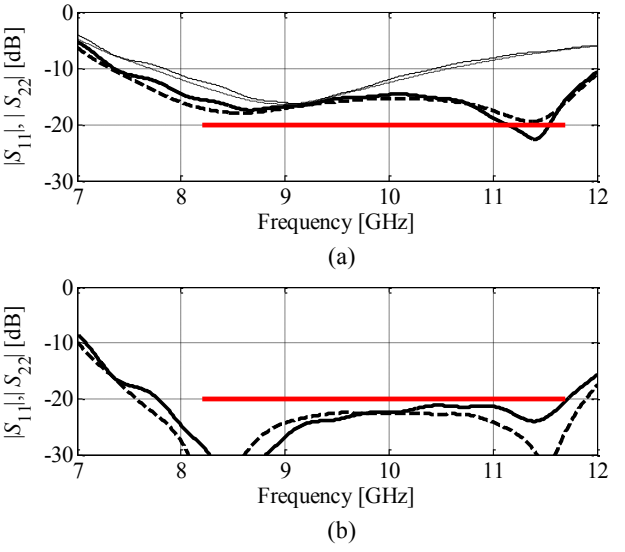

Fig. 3.35 CBCPW-to-SIW transitions, $|S_{11}|$ (solid) and $|S_{22}|$ (dash): (a) the initial (thin) and optimized (thick) design without protruding vias; and (b) optimized design with two vias.

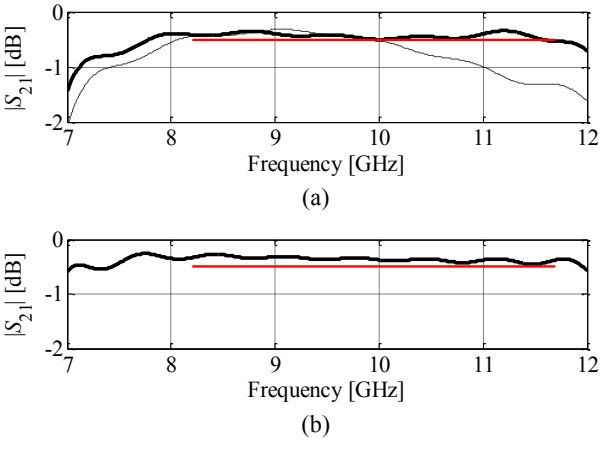

Fig. 3.36 CBCPW-to-SIW transitions, $|S_{21}|$: (a) the initial (thin-dash) and optimized (thick-solid) design without protruding vias; (b) optimized design with two vias.

Table 3.9 CPW-SIW transitions: final designs

Parameter [mm]	Design 1 (no extra vias)	Design 2 (two extra vias)
l_1	0.695	0.570
l_2	7.451	7.389
l_3	0.323	0.323
w_1	2.387	2.387
s_1	0.764	0.839
s_2	0.235	0.235
r_0	0.250	0.250
r_1	-	0.313
x_1	-	1.750
y_1	-	11.375
h_1	-	1.355
$\|S_{11}\|$,$\|S_{22}\|$ [dB]	<= –14.6	<= –20
Bandwidth [GHz]	8.0–11.75	7.78–11.72

3.6 Conclusion

In this chapter, several techniques for computationally efficient simulation-driven design optimization of microwave structures have been discussed. We also presented a number of design examples concerning various microwave components, including microstrip filters, planar antennas, as well as transition structures. In all cases, the surrogate-based techniques presented in the previous chapter have been employed as optimization engines. The results presented here indicate that the surrogate-based optimization methods make the simulation-driven microwave design feasible and efficient, both in terms of the quality of the final design, and in terms of the computational cost. In most cases, the design cost corresponds to a few high-fidelity electromagnetic simulations of the microwave structure under consideration, typically comparable to the number of design variables. While this kind of performance is definitely appealing, improved robustness and reliability as well as availability through commercial software packages are needed to make the surrogate-based techniques widely accepted by microwave engineering community. Therefore, a substantial research effort in this area is expected in the years to come.

References

1. Bandler, J.W., Cheng, Q.S., Dakroury, S.A., Mohamed, A.S., Bakr, M.H., Madsen, K., Søndergaard, J.: Space mapping: the state of the art. IEEE Trans. Microwave Theory Tech. 52, 337–361 (2004)
2. Director, S.W., Rohrer, R.A.: The generalized adjoint network and network sensitivities. IEEE Trans. Circuit Theory CT-16, 318–323 (1969)
3. CST Microwave Studio, ver. 20109, CST AG. Bad Nauheimer Str.,19, D-64289, Darmstadt, Germany (2010)

4. HFSS, release 13.0, ANSYS (2010), http://www.ansoft.com/products/hf/hfss/
5. Queipo, N.V., Haftka, R.T., Shyy, W., Goel, T., Vaidynathan, R., Tucker, P.K.: Surrogate based analysis and optimization. Progress in Aerospace Sciences 41, 1–28 (2005)
6. Forrester, A.I.J., Keane, A.J.: Recent advances in surrogate-based optimization. Prog. in Aerospace Sciences 45, 50–79 (2009)
7. Koziel, S., Bandler, S.W., Madsen, K.: A space mapping framework for engineering optimization: theory and implementation. IEEE Trans. Microwave Theory Tech. 54, 3721–3730 (2006)
8. Koziel, S., Meng, J., Bandler, J.W., Bakr, M.H., Cheng, Q.S.: Accelerated microwave design optimization with tuning space mapping. IEEE Trans. Microwave Theory and Tech. 57, 383–394 (2009)
9. Koziel, S.: Shape-preserving response prediction for microwave design optimization. IEEE Trans. Microwave Theory and Tech. 58(11), 2829–2837 (2010)
10. Koziel, S., Ogurtsov, S.: Robust multi-fidelity simulation-driven design optimization of microwave structures. In: IEEE MTT-S Int. Microwave Symp. Dig, Anaheim, CA, pp. 201–204 (2010)
11. Koziel, S.: Efficient optimization of microwave structures through design specifications adaptation. In: IEEE Int. Symp. Antennas Propag. Toronto, Canada (2010)
12. Koziel, S., Cheng, Q.S., Bandler, J.W.: Implicit space mapping with adaptive selection of preassigned parameters. IET Microwaves, Antennas & Propagation 4, 361–373 (2010)
13. Pozar, D.M.: Microwave Engineering, 3rd edn. Wiley, Chichester (2004)
14. Koziel, S., Bandler, J.W., Madsen, K.: Quality assessment of coarse models and surrogates for space mapping optimization. Optimization Eng. 9, 375–391 (2008)
15. Koziel, S., Bandler, J.W.: Space-mapping optimization with adaptive surrogate model. IEEE Trans. Microwave Theory Tech. 55, 541–547 (2007)
16. Swanson, D., Macchiarella, G.: Microwave filter design by synthesis and optimization. IEEE Microwave Magazine 8(2), 55–69 (2007)
17. Rautio, J.C.: EM-component-based design of planar circuits. IEEE Microwave Magazine 8(4), 79–90 (2007)
18. Cheng, Q.S., Bandler, J.W., Koziel, S.: Space mapping design framework exploiting tuning elements. IEEE Trans. Microwave Theory and Tech. 58(1), 136–144 (2010)
19. Koziel, S., Bandler, J.W., Cheng, Q.S.: Design optimization of microwave circuits through fast embedded tuning space mapping. In: European Microwave Conference Paris, Septemper 26– October 1 (2010)
20. Cheng, Q.S., Rautio, J.C., Bandler, J.W., Koziel, S.: Progress in simulator-based tuning—the art of tuning space mapping. IEEE Microwave Magazine 11(4), 96–110 (2010)
21. Alexandrov, N.M., Dennis, J.E., Lewis, R.M., Torczon, V.: A trust region framework for managing use of approximation models in optimization. Struct. Multidisciplinary Optim. 15, 16–23 (1998)
22. Salleh, M.H.M., et al.: Quarter-wavelength side-coupled ring resonator for bandpass filters. IEEE Trans. Microwave Theory Tech. 56, 156–162 (2008)
23. FEKO User's Manual. Suite 5.5, EM Software & Systems-S.A (Pty) Ltd, 32 Techno Lane, Technopark, Stellenbosch, 7600, South Africa (2009)
24. Agilent ADS, Version 2009, Agilent Technologies, 395 Page Mill Road, Palo Alto, CA, 94304 (2009)

25. Koziel, S., Bandler, J.W., Cheng, Q.S.: Robust trust-region space-mapping algorithms for microwave design optimization. IEEE Trans. Microwave Theory and Tech. 58, 2166–2174 (2010)
26. Liao, C.-K., Chi, P.-L., Chang, C.-Y.: Microstrip realization of generalized Chebyshev filters with box-like coupling schemes. IEEE Trans. Microwave Theory Tech. 55, 147–153 (2007)
27. Sonnet em. Ver. 12.54, Sonnet Software. North Syracuse, NY (2009)
28. Koziel, S., Bandler, J.W.: Automated tuning space mapping implementation for rapid design optimization of microwave structures. In: Int. Review of Progress in Applied Computational Electromagnetics, ACES 2009, pp. 138–143 (2009)
29. Guan, X., Ma, Z., Cai, P., Anada, T., Hagiwara, G.: A microstrip dual-band bandpass filter with reduced size and improved stopband characteristics. Microwave and Opt. Tech. Lett. 50, 618–620 (2008)
30. Qing, X.M., Chen, Z.N.: Antipodal Vivaldi antenna for UWB applications. In: European Electromagnetics Symposium, UWB SP 7 (2004)
31. SMA Edge Mount P.C. Board Receptacles. Online Catalog, Applied Engineering Products, http://aepconnectors.com/pdf/SMAedg.pdf
32. Beachkofski, B., Grandhi, R.: Improved distributed hypercube sampling. American Institute of Aeronautics and Astronautics, Paper AIAA, 2002–1274 (2002)
33. Koziel, S., Ogurtsov, S.: Computationally Efficient Simulation-Driven Design of a Printed 2.45 GHz Yagi Antenna. Microwave and Optical Technology Letters 52, 1807–1810 (2010)
34. Chen, C.A., Cheng, D.K.: Optimum element lengths for Yagi-Uda arrays. IEEE Trans. Antennas Propag. 23, 8–15 (1975)
35. Cheng, D.K., Chen, C.A.: Optimum element spacings for Yagi-Uda arrays. IEEE Trans. Antennas Propag. 21, 615–623 (1973)
36. Balanis, C.A.: Antenna theory: analysis and design. Wiley-IEEE Press, Chichester (2005)
37. Chen, Z.N.: Wideband microstrip antennas with sandwich substrate. IET Microw. Ant. Prop. 2, 538–546 (2008)
38. Gupta, K.C., Garg, R., Bahl, I., Bhartia, P.: Microstrip lines and slotlines, 2nd edn. Artech House, Norwood (1996)
39. Simons, R.N.: Coplanar waveguide circuits, components, and systems. Wiley, Chichester (2001)
40. Cheng, Q.S., Bandler, J.W., Koziel, S., Bakr, M.H., Ogurtsov, S.: The state of the art of microwave CAD: EM-based optimization and modeling. Int. J. RF and Microwave Computer-Aided Eng. 20, 475–491 (2010)
41. Burke, J.J., Jackson, R.W.: Surface-to-surface transition via electromagnetic coupling of microstrip and coplanar waveguide. IEEE Trans. Microwave Theory Tech. 37, 519–525 (1989)
42. Kolda, T.G., Lewis, R.M., Torczon, V.: Optimization by direct search: new perspectives on some classical and modern methods. In: SIAM Review, vol. 45(3), pp. 385–482 (2003)
43. Wu, K.: Substrate Integrated Circuits (SiCs) – A new paradigm for future Ghz and Thz electronic and photonic systems. IEEE Circuits and Systems Society Newsletter 3(2) (2009)
44. Collin, R.E.: Foundation for Microwave Engineering, 2nd edn. Wiley-IEEE Press, Chichester (2000)
45. Koziel, S., Cheng, Q.S., Bandler, J.W.: Space mapping. IEEE Microwave Magazine 9(6), 105–122 (2008)

46. Ogurtsov, S., Koziel, S., Rayas-Sánchez, J.E.: Design optimization of a broadband microstrip-to-SIW transition using surrogate modeling and adaptive design specifications. In: International Review of Progress in Applied Computational Electromagnetics, Tampere, Finland. ACES, pp. 878–883 (2010)
47. Koziel, S.: Adaptively adjusted design specifications for efficient optimization of microwave structures. Progress in Electromagnetic Research B (PIER B) 21, 219–234 (2010)